Numerical simulation of sampling capabilities of spiral trajectory and echo-planer imaging in magnetic resonance fingerprinting

By

Samuel Melke

In partial fulfillment of the requirements for the degree of Master of Science in Biomedical Engineering

Center of Biomedical Engineering

Addis Ababa Institute of Technology

Addis Ababa University

Advisor: Dawit Assefa Haile (PhD)

January 2023

Addis Ababa, Ethiopia

Declaration

I, the undersigned, declare that this thesis and the work presented in it are my own and have been generated by me as the result of my original research.

I confirm that:

- This work was done wholly or mainly while in candidature for a research degree at this university.
- Where any part of this thesis has previously been submitted for a degree or any other qualification at this university or any other institution, this has been clearly stated;
- Where I have quoted from the work of others, the source is always given. Except for such quotation, this thesis is entirely my work;
- I have acknowledged all main sources of help;
- This work or any part of this work has not been published before submission;

Name: ____________________

Signature: ____________________

Date: ____________________

This MSc thesis has been submitted for examination with my approval as an advisor.

____

Dawit Assefa Haile (PhD)

Addis Ababa University

School of Graduate Studies

Certificate of Examination

This is to certify that the thesis prepared by Samuel Melke entitled: **Numerical simulation of sampling capabilities of spiral trajectory and echo-planer imaging in magnetic resonance fingerprinting** submitted in partial fulfillment of the requirements for the degree of Master of Science in Biomedical Engineering (Bioinstrumentation & Imaging) complies with the regulations of the University and meets the accepted standards for originality and quality.

Signed by the examining committee

Examiner: ____________________________Sig.: _____________ Date _______________
(internal)

Examiner: ____________________________Sig.: _____________ Date ________________
(external)

____

Graduate program director

Abstract

Magnetic Resonance Fingerprinting (MRF) is a novel method proposed to solve the limitations of quantitative Magnetic Resonance Imaging (qMRI). One of the ways MRF accelerates data acquisition is by using various sampling mechanisms to undersample the k-space. In this thesis, the effectiveness of spiral sampling and accelerated cartesian sampling using multi-shot Echo-Planar Imaging (EPI) are compared by keeping the other steps in the MRF framework constant. Dictionary atoms were generated by using Bloch simulation. During the data acquisition, a realistic simulation framework based on the Bloch equation is built and implemented in a MATLAB platform. An inversion-recovery balanced steady-state free precession sequence was used in simulating the series images as well as the dictionary. The dot product of the simulated signal evolution and the dictionary of predicted signal evolutions is used for pattern matching. To check the efficacy of the methodology, cylindrical and brain numerical phantoms were used. The respective percentage errors in T1, T2 and off-resonance quantification were 2.6%, 2.3%, and 14% for spiral-MRF and 39%, 43%, and 124% for EPI-MRF. The results showed that spiral undersampling produces superior results in a close match with the ground truth compared to multi-shot EPI, showing the great promises of spiral trajectory to be used as an effective sampling tool in MRF. The MRF simulator developed in this thesis work effectively simulates the image acquisition process of an MRI machine and has consistently produced accurate results. The obtained results are generally comparable to those reported in other studies that utilized real scanners.

Acknowledgment

First of all, I would like to thank God Almighty for giving me the strength, knowledge, and opportunity to do this thesis. It gives me immense pleasure to thank my advisor Dr. Dawit Assefa Haile for his continued support, guidance, meticulous suggestions, and astute criticism thorough out this work. I am grateful for Prof. AbdEl-Monem El-Sharkawy for his mentorship during my research visit at Cairo University. I am grateful to my colleagues at the Center of Biomedical Engineering for all the support they gave me. I would like to express my sincere thanks to Addis Ababa University for sponsoring my study. My deepest gratitude to the African Biomedical Engineering Mobility (ABEM) project funded by the Intra-Africa Academic Mobility Scheme of the Education, Audiovisual and Culture Executive Agency of the European Commission for financing my stay at Cairo university as a visiting research student.

Dedication

I dedicate this work to my family.

Table of Contents

List of figures

List of tables

List of abbreviations

AI	Artificial Intelligence
BW	Bandwidth
CSF	Cerebrospinal fluid
df	off-resonance frequency
EPI	Echo-Planar Imaging
FA	Flip Angle
FID	Free Induction Decay
FOV	Field of View
GM	Grey Matter
GT	Ground Truth
IR-bSSFP	Inversion Recovery balanced Steady-State Free Precession
MR	Magnetic Resonance
MRF	Magnetic Resonance Fingerprinting
MRI	Magnetic Resonance Imaging
PD	Proton Density
qMRI	quantitative Magnetic Resonance Imaging
RF	Radiofrequency
SVD	Singular Value Decomposition
TE	Echo Time
TR	Repetition Time
TruFISP	True Fast Imaging with Steady State Precession
WM	White Matter

Chapter 1: Introduction

1.1 Background

When we usually talk about quantitative analysis in imaging modalities other than MRI, we are referring to some type of numerical study performed on images as opposed to qualitative study performed on the images through visual inspection. In Magnetic Resonance Imaging (MRI) studies, however, quantitative imaging is a completely different concept. Quantitative MRI (qMRI) refers to getting maps of meaningful biophysical properties of tissues that can be measured in physical units. For example, when we say a T1 map in qMRI, we are not talking about mere intensity values in the image (like what we do in conventional MRI) but rather the T1 values of the pixels, which are assumed to represent a particular tissue, in units of time [1].

Although there are some quantitative MR methods that are currently being used in diagnosis and treatment of various abnormalities, most of today's clinical MR images are qualitative that rely on the acquisition of weighted images. The contrast of weighted images is the result of a variety of variables interacting to create the image. The contrast could be affected by the tissue's biophysical properties, the physical parameters of the MRI machine, and exogenous substances that are ingested into the tissue (contrast agents). Despite its significant role in clinical diagnosis and monitoring, qualitative MRI is only capable of detecting gross morphological abnormalities or local abnormalities that cause regional disparities in signal intensity. Qualitative MRI depends on contrast variations between the "affected" region and the "normal" one to diagnose diseases. Hence, qualitative MRI has decreased sensitivity to global changes [2].

The biophysical properties of tissues such as T1 and T2 are useful for detecting abnormalities in our body such as cancer and epilepsy [3, 4, 5]. qMRI can aid in the detection of these tissue properties. Although extremely valuable, qMRI is not widely used in clinical practice due to the long acquisition time of quantitative maps. In the past few years, there have been several rapid quantitative imaging techniques proposed [6, 7]. Although these methods are fast, their reproducibility and repeatability need to be improved [8, 9].

Magnetic Resonance Fingerprinting (MRF) proposed in [10] is a novel quantitative technique that has shown great potential to simultaneously and efficiently obtain multiple parameter maps including T1 and T2. Unlike other qMRI techniques, MRF is fast and it can detect more than one parameter at a time which will save time otherwise will be spent on mapping each physical property individually. MRF has three major components. The first step is acquiring a dataset with randomized repetition times (TR) and flip angles (FA). Then a dictionary containing all possible signal evolution of relevant T1 and T2 values is constructed. Finally, there is a pattern recognition process where parameter maps are generated by a pixel-wise template matching between the acquired data and the dictionary.

Computer simulation of physical processes is a valuable tool to predict the behavior and the outcome of a real-world system. Because they allow checking the reliability of a proposed method before in vivo experiments, computer simulations have become an integral part of scientific studies. Over the years, simulators for MRI using the famous Bloch equation [11] have been developed [12, 13, 14, 15, 16]. These simulators aid in pulse sequence design, reconstruction algorithm design, understanding artifacts in images, and education. Early simulators used simple analytical signal expressions for the MRI process to develop and test new pulse sequences and to produce contrast images. Nowadays, with the increasing complexity of MR systems and the development of new acquisition techniques, more realistic simulators have been proposed [17]. Most recent simulators take advantage of new emerging technologies such as high-performance computing to decrease the time needed to acquire data.

One way of accelerating the data acquisition process in MRF is by undersampling the k-space (Fourier space). MRF using different techniques of sampling k-space (trajectories) such as spiral, radial and echo-planar imaging (EPI) has been proposed [10, 18, 19]. Spiral sampling is used widely in most current MRF methods.

The main aim of this thesis is to compare the undersampling capabilities of spiral and EPI techniques in the data acquisition step of MRF by keeping other factors constant. With this intention, a numerical simulation framework that can accurately simulate a two-dimensional MRI data acquisition and MRF dictionary generation is built. Data acquisition using the two sampling techniques is simulated. A pattern matching algorithm that matches the acquired data with the predicted dictionary is built and used. The performance of the two techniques is measured by comparing their respective maps with the phantom (ground truth) images and with each other.

1.2 Problem Statement

MRF is a new and promising quantitative technique. Currently, there is an immense ongoing research effort to make the technique more useful in clinical practice. Although several independent research using different sampling techniques in the data acquisition step of MRF have been proposed, there is no work on realistic numerical simulation to compare EPI and spiral trajectories in the context of MRF. The development and optimization of a new MRI method is a repetitive process that needs modifications of many variables until the desired result is obtained. This process is tedious, time-consuming, and expensive and often needs a phantom or human subject to test it on a real scanner and observe the results. Making an open source MRF simulator available will assist in reducing the initial effort researchers put into reinventing the wheel to simulate their methods. As far as the literature review carried out in the current thesis work is concerned, there are no such simulation tools for MRF available.

1.3 Objective of the Thesis

1.3.1 General objective

The main objective of this thesis is to measure and compare the effectiveness of spiral undersampling and multi-shot echo-planar imaging in producing accurate quantitative maps (images) of tissue properties using numerical simulation implemented in MATLAB platform.

1.3.2 Specific objectives

The specific objectives of this thesis are:

- To build and test a realistic numerical MRI simulator;
- To build a dictionary of estimated signal evolutions for a given T1, T2, off-resonances, and proton density (PD) values;
- Simulate the signal acquisition for a single-shot spiral sampling and sixteen-shot echo-planar imaging;
- Perform pattern matching between the acquired signal and the dictionary entries to build quantitative maps of T1, T2, and off-resonance frequency, and
- Compare the performance of the two sampling trajectories in producing accurate maps of the biophysical properties of tissue.

1.4 Significance of the Thesis

Since the introduction of MRF in 2013 [10], there has been an increasing research interest in the method. There are a multitude of factors involved in this technique and the potential for further investigation is huge. One of the areas that need improvement in MRI in general and MRF in particular is the way the k-space is sampled (k-space trajectory). MRF's inherent nature of not being affected by undersampling artifacts and noise provides a huge opportunity for further investigation into techniques of sparse imaging. Sparse sampling together with robust reconstruction methods will reduce the time required for data acquisition. Therefore, the investigation of different trajectories in k-space, which this thesis aims to do, will aid in further improving the accuracy and speed of MRF.

Numerical simulation of MRI experiments on a computer is a valuable tool for predicting the outcomes of a proposed method before in vivo experiment. This will help save the time, energy, and resources that would have been spent on a real in vivo experiment using highly expensive MR machines at the initial stage of research. Therefore, using such a tool nowadays is not an option but a necessity while working on MR research. If such tool is readily available, it could help save the effort researchers would put into reinventing the wheel and hence contributes to fast testing and prototyping. The importance of MRI simulators in teaching is also paramount. The feasibility of such MRF simulations like the one we have built in this thesis on a simple personal computer will save researchers a tremendous amount of time, resources, and effort. This tool can serve as a flexible, readily available, and expandable platform for easily customizing virtual MRF experiments in the development of new MRF methods.

This thesis also confirms the validity of MRF in quantitative imaging. It further will help assess and compare the effectiveness of spiral and EPI methods of sampling k-space in the acquisition of MRF images in the cases of dot product based pattern matching.

1.5 Scope and Delimitations of the Thesis

This thesis models acquisition and reconstruction of MRF images for a two-dimensional tissue assuming a perfect excitation of a single slice of a rectangular cross-sectional region. The effect of radiofrequency (RF) pulse inhomogeneity is not considered. This work is based on the single isochromatic method proposed previously in the literature [20]. Both the flip angle and off-resonance frequency are assumed to be essentially homogeneous inside a voxel. No data was collected on a real scanner to test the methodology.

1.6 Organization of the Thesis

The rest of the thesis is organized into the following chapters. In Chapter 2, the basic concepts and physics of magnetic resonance imaging as well as the Bloch equation are discussed. Chapter 3 presents basic concepts of magnetic resonance fingerprinting including related works and applications. Chapter 4 explains the methodologies and materials employed in this thesis including tools used, sampling mechanisms, reconstruction algorithms, and pattern matching while Chapter 5 presents selected results accompanied by useful discussions. Chapter 6 offers a summary and discussion of the research findings in this thesis, their implications as well as recommendations for possible future research.

Chapter 2: Magnetic Resonance Imaging

2.1 Introduction

This chapter gives a brief introduction to MRI including physics and imaging.

Nuclear magnetic resonance is a process by which certain atomic nuclei, when placed within a magnetic field, absorb or emit energy in the radiofrequency range of the electromagnetic spectrum. MRI is the application of nuclear magnetic resonance to medical imaging. The term ‘magnetic’ in its name refers to the use of magnetic fields and resonance refers to the need to match the frequency of the oscillating magnetic field to the ‘precessional’ frequency of the spin of some nucleus (hence ‘nuclear’) in a tissue. The basic idea that led to the invention of MRI is the discovery of the fact that the intrinsic angular momentum (or ‘spin’) of a proton in a magnetic field precesses about that field at the ‘Larmor frequency’ which, in turn, depends linearly on the magnitude of the field itself. If a spatially varying magnetic field is introduced across the object, the Larmor frequencies are also spatially varying. The different frequency components of the signal could be separated to give spatial information about the object. The discovery of spatially encoding the data opened the door to MR imaging.

MRI is a new and rapidly growing discipline in the field of applied sciences. The main advantage of MRI is the imaging of soft tissues in the human body and metabolic processes therein, because of which it occupies a strong position in biomedical science applications. MRI is a useful imaging machine because of its sensitivity to a broad range of tissue properties which are the main indicators of tissue health. One of the main reasons that make MRI preferred is its safety in that it does not use any ionization energy and can provide a diagnosis of conditions in our body noninvasively. It can be applied to people of any age. Another significance is the arbitrary positioning of the imaging plane. MRI can also give functional information about the body.

Clinical applications of MRI encompass clinical neurology, cardiology, cancer, and soft tissue damages. It can be used to detect anomalies in the brain and spinal cord [21]. It assists in the detection of tumors, cysts, and other anomalies in various parts of the body [22, 23]. Screening for women who face a high risk of breast cancer is done using MRI [24]. It can also be used to find injuries or abnormalities of the joints, certain types of heart problems, and diseases of the liver and other abdominal organs [25, 26, 27]. MRI is also used for the evaluation of pelvic pain in women and uterine anomalies in women undergoing evaluation for infertility [28, 29]. In clinical neurology, it has been applied to classification of brain tissues, measuring volumes of brain structures, multiple sclerosis, neurodegeneration, and stroke. MRI has been in use to detect breast, colorectal, liver, prostate, and other types of cancers [30].

2.2 MRI Basics

Atoms with an odd number of protons possess a nuclear spin angular momentum and therefore exhibit the MR phenomenon. These MR-relevant nuclei are usually referred to as spins. In biological specimens, hydrogen (^1H), with a single proton, is the most abundant, the most sensitive, and by far the most studied. The nature of MR is based on the interaction of these spins with three types of magnetic fields: 1) static field B_o, 2) radiofrequency field B_1 and 3) linear gradient fields G_x, G_y, and G_z in the x, y, and z directions respectively.

2.2.1 Static field B_0

In the absence of an external magnetic field, the spins are oriented randomly and the net macroscopic magnetic moment is zero. However, in the presence of an external magnetic field B_o, two major effects occur. First, the magnetic moment vectors tend to align in the direction of B_0 to create a net magnetic moment (See Fig. 2.1). By convention, the direction of the applied field is called the *z*-direction or longitudinal direction. Second, the nuclear spins exhibit resonance at a well-defined frequency called the Larmor frequency ω_0. This Larmor frequency and the applied magnetic field are related by the following equation,

$$\omega_0 = \gamma B_0 \tag{2.1}$$

or

$$f = \frac{\gamma}{2\pi} B_0 \tag{2.2}$$

where γ is called the gyromagnetic ratio, a known constant unique for each type of atom.

From Eqn. 2.1 it can be seen that the precessional frequency of a spin is affected by the gyromagnetic ratio of the spin and the applied external magnetic field. In MR this condition of the atom being aligned with the external static magnetic field and precessing at the Larmor frequency is known as the equilibrium condition of magnetization.

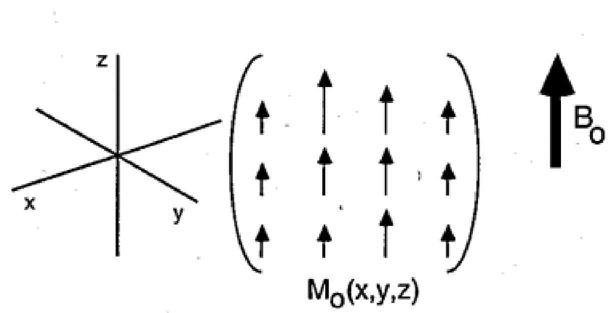

Figure 2. 1: *Equilibrium condition of magnetization (Mo (x,y,z)) in the presence of the static magnetic field Bo [31].*

2.2.2 Radiofrequency Field B_1

The application of the static magnetic field in MRI causes the spins to align in the z-direction, resulting in a net magnetic moment. While the magnetic field from the spin system is much weaker than the main magnetic field, we can measure the net magnetic moment by flipping the spins to a transverse direction. To do this another field called the radiofrequency (RF) magnetic pulse B_1 tuned to the resonant frequency of the spins is applied in the xy (transverse) plane to excite these spins out of equilibrium (Fig. 2.2 a). Effectively, B1 applies a torque that rotates the magnetization vectors by a prescribed angle dependent on the strength. Now we can detect the total magnetic field from the volume of a body part.

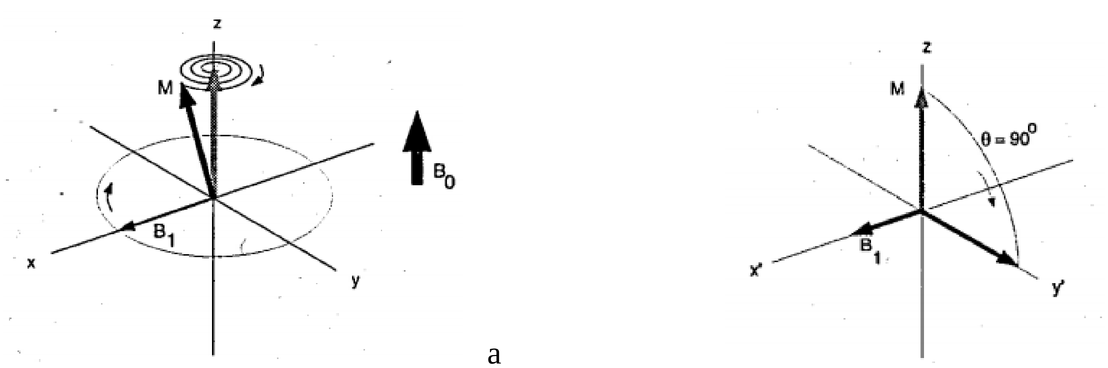

Figure 2. 2: *Excitation of the equilibrium magnetic field with* (a) *the application of radiofrequency pulse (b)* 90^0 *flip angle [31].*

If the excitation is set for (say) a 90^0 tip angle (Fig. 2.2 b), then upon turning the excitation off, the tipped vectors precess in the xy plane at the Larmor frequency. Relaxation back to equilibrium also occurs in which the length of the magnetization vector does not remain constant over time. The time constant characterizing the return of the magnetization vector along the z-axis (longitudinal axis) is called T_1, while the time constant characterizing the decay of the vector component in the xy plane (transverse plane) is called T_2. In humans, T_1 values of most tissues range from about 100-1500ms while T_2 values range from about 20-300ms [32]. These relaxation time constants, along with the density of the atoms (PD), are important MR parameters that have distinct values for different tissues.

From Faraday's law of induction, the rotating magnetization vectors induce an electromotive force (EMF) in an RF receiver coil oriented to detect changes in magnetization in the xy plane. Often, the coil generating the RF excitation field will switch modes and receive the signal as well. The generated time signal is called free induction decay (FID); in general, a set of FIDs will be recorded and processed to reconstruct an MR image.

2.2.3 Linear Gradient Fields (G_x, G_y, G_z)

If the applied field is only the static field B_0 in the z–direction, then all spins possess the same resonance frequency ω_0 and, if excited, behave like oscillators inducing signals at that frequency. Because the excitation/receiver RF coil encompasses the entire region of interest, it is not possible to excite a selected portion of the volume nor is it possible to distinguish the signals generated from different spatial locations if only B_0 exists. The problem lies in the fact that we record the total signal generated by all the oscillators of the excited region in a single time waveform. Our next step will be to determine which signal came from which voxel not just the whole magnetic moment of a volume of tissue. To do so we use the so-called gradient pulses which are a type of magnets used for the localization of the signals from our body.

There are three kinds of gradient pulses in MR: the slice select gradient in the direction of the main magnetic field (z direction), the frequency encoding gradient in the x direction, and the phase encoding gradient in the y direction. The slice gradient also known as the z gradient is a magnetic field applied in the z-direction with the sole purpose of varying the frequency of precession of the spins along the z-direction so that the RF pulse tuned to a particular frequency will excite or flip only a selected slab of spins that we call a slice. After we flipped the specific spin at a particular longitudinal distance, we now have a plane of spins producing a net magnetization in the transverse plane. We then have to distinguish from where within the plane the signal comes. To do so we use two gradients applied in the x and y directions. The y gradient is applied first to make the spin frequency vary along y after some time we turn the y gradient off. Now the spins will return to their normal precession frequency but will have different phases, hence the name phase encoding gradient. The spins along x are still precessing at the same frequency and phase. Now we apply the x gradient and make their frequency vary with their position. At the same time, we sample the signal using our analog-to-digital converter to record the signal.

For example, when we apply a gradient G_z in the z-direction ($G_z z$), then the applied field is $B_0 + G_z z$. Now the field strength varies with z-location; hence, $G_z = dB_z/dz$. The frequency of the spins thus becomes a function of their z-location; that is, $\omega(z) = \gamma(B_0 + G_z z) = \omega_0 + \gamma G_z z$.

The idea of purposefully creating an inhomogeneous field with a gradient plays a vital role in MR imaging. By making the magnetic field inhomogeneous, we take advantage of the fact that the resonant frequency of these nuclei is proportional to the applied field strength and that this frequency changes instantaneously when the field strength changes.

2.3 Conventional MRI Methods

MR imaging methods consist of two major steps: excitation and reception. Each excitation/reception sequence results in a time signal measurement that provides a single spatial projection of the object under study. A typical data acquisition duration is about 10 milliseconds. After pausing for some time (often 0.1 – 0.2s) to allow suitable magnetization recovery, the excitation/reception sequence repeats for the collection of the next measurement. A set of measurements is thus collected to provide an appropriate set of projections for image reconstruction.

Combinations of excitation pulses are typically employed to make the amplitude of these oscillators become some function of the MR parameters (PD, T1, T2, diffusion) to create a contrast between tissues. This results in different images that are principally influenced by one MR parameter (property of tissue) like T1 weighted, T2 weighted, diffusion-weighted images, etc.

2.3.1 Selective excitation

If the RF magnetic field B1 is applied in the presence of B_0 only, then all spins are at the same resonance frequency and the excitation is nonselective because all spins are tipped. In this case, where the entire volume contributes signal, some form of 3D imaging must be performed.

Hence it is desirable to be able to reduce a 3D imaging task into a manageable 2D one by exciting a plane instead of the entire volume. Such selective excitation is achieved by applying B1 in the presence of Bo and a linear gradient field. If we wish to excite a plane, say, perpendicular to the z-axis of thickness Δz, then G_z turns on during the RF excitation. With G_z on, the resonance frequency varies linearly with the z-position. B_1 must now possess a temporal frequency bandwidth that matches the bandwidth of resonance frequencies of spins in the slice of interest (Fig. 2.3). The desired bandwidth is $\gamma G_z \Delta z$, centered about ω_0 for excitation of the plane at $z = 0$.

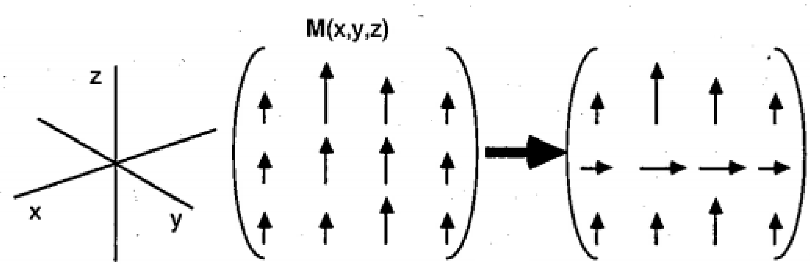

***Figure 2. 3**: Selective excitation [31].*

2.3.2 Frequency encoding and phase encoding

The process of frequency encoding and phase encoding in MRI is used to obtain spatial information in the transverse plane, which is one of the three-dimensional planes used to define the spatial location of the MRI signal. In phase encoding, a magnetic gradient field is applied along the y-direction, which results in different phases of precession for hydrogen protons located at different positions along the y-direction. The phase encoding gradient is turned on briefly before the signal acquisition process begins and results in a gradient in the phase of the MRI signal along the y-direction.

In frequency encoding, a magnetic gradient field is applied along the x-direction, which results in different frequencies of precession for hydrogen protons located at different positions along the x-direction. The frequency encoding gradient is applied during the signal acquisition process and produces a gradient in the frequency of the MRI signal. Together, frequency encoding and phase encoding allow for the creation of a two-dimensional image in the transverse plane.

By applying a series of gradient fields along the x and y-directions and varying the amplitude and duration of these gradients, the position of the hydrogen protons in the transverse plane can be encoded with high spatial resolution. This spatial information is then used to reconstruct a two-dimensional image of the body's internal structures using the Fourier transform.

2.3.3 2D Imaging methods

To perform 2D imaging we follow the following steps. We apply a selective excitation in the presence of G_z such that nuclear magnetization vectors in a thin plane at a particular z-location are tipped into the xy plane. The excited spins, acting as RF sources, have an amplitude distribution $M(x, y)$ that we wish to image. As the excited spins precess and induce an EMF in the receiver coil, we encode their signals via gradient fields to get spatially dependent information in the FID signal. Eventually, the signal decays and the spin vectors return to equilibrium. We then repeat this procedure to acquire the next measurements.

2.3.4 k-space in MRI

In MRI, the k-space data is collected by applying magnetic gradients to the body and measuring the resulting change in magnetic field. The local spatial distribution of spins can be determined from the frequency content of the MR signal resulting from the fact that identical nuclei precess at different rates in locations where the magnetic field has changed. This process can be modeled mathematically as a Fourier transform of the spatial distribution of the magnetic signals in the body. The k-space data is represented as a complex matrix, with each element of the matrix representing the amplitude and phase of the signal at a specific location in k-space.

The Fourier transform can be written mathematically as:

$$F(k_x, k_y, k_z) = \iiint f(x, y, z) e^{-2\pi i (k_x x + k_y y + k_z z)} dx dy dz \tag{2.3}$$

where $F(k_x, k_y, k_z)$ represents the k-space data, $f(x, y, z)$ represents the spatial distribution of magnetic signals in the body, (k_x, k_y, k_z) are the spatial frequency components in the k-space, and (x, y, z) are the spatial coordinates in the image space. The Fourier transform maps the signals in image space to k-space and vice versa, making it possible to go back and forth between the two representations.

After acquiring the k-space data, it is processed using inverse Fourier transform to generate an image of the internal structures of the body. The inverse Fourier transform can be written as:

$$f(x, y, z) = \frac{1}{V} \iiint F(k_x, k_y, k_z) e^{2\pi i (k_x x + k_y y + k_z z)} dk_x dk_y dk_z \tag{2.4}$$

where V is the volume of the sample and $f(x, y, z)$ represents the image data in image space, which is the final output of the MRI scan.

2.4 Bloch Equation

The Bloch equations are a set of phenomenological equations in nuclear magnetic resonance imaging discovered by Felix Bloch in 1946 [11]. They are used to calculate the nuclear magnetization $M = (Mx, My, Mz)$ as a function of time when relaxation times T_1 and T_2 are present. To understand them we need to start from the atomic level.

The nuclei that have odd atomic numbers or/and odd atomic weights possess an angular moment $\vec{J}$ called spin, which can be visualized as a microscopic magnet rotating clockwise around its own axis with a magnetic moment μ. Assuming that the static magnetic field of strength B_0 is applied in the z-direction, with the coordinates (x, y and z), the spin experiences a torque that rotates the spin around the direction of B_0.

$$\frac{d\mu}{dt} = \gamma\mu \times B_0 \tag{2.5}$$

where $\times$ is cross product

the solution of Eqn. 2.5 in the x-y plane is:

$$\mu_{xy}(t) = \mu_{xy}(0)\, e^{-\gamma B_0 t} \tag{2.6}$$

which describes a clockwise rotation or precession of $\vec{\mu}$ about the direction of the B_0 field (Eqn. 2.1). For a spin system in an object, the bulk magnetization is the vector sum of all the microscopic spins:

$$M = \sum_{N_s} \mu \tag{2.7}$$

where N_s is the total number of nuclei in the object to be imaged.

There is an excess number of H^1 spins that align up than align down with the B_0 field, so the collective effect of the spin system generates an observable bulk magnetization vector M that is pointing along the direction of B_0.

The RF pulse that is added to induce transverse magnetization can be described by the equation:

$$B_1(t) = B_1^e(t)e^{-i(\omega_{rf}t+\varphi)} \tag{2.8}$$

where $B_1^e(t)$ is the pulse envelope function, ω_{rf} is the oscillating frequency of the RF pulse and φ is the phase of the RF pulse. In the case of an on-resonance excitation, when $\omega_{rf} = \omega_0$ and the phase of the RF pulse is constant, the RF pulse is simplified as

$$B_{1,rot} = B_1^e(t)i \tag{2.9}$$

where $B_{1,rot}$ is the RF pulse expressed in the rotational frame, which is rotating about the z-axis with the frequency of ω_0. The coordinates systems for this frame (rotational frame of reference) are defined by x', y', z' with the directional units of $i, j,$ and k respectively.

This excitation with an RF pulse rotates the M vector away from the z'-axis with a precession angle or flip angle (FA) of:

$$\alpha = \int_0^{\tau_p} \gamma\, B_1^e(t)dt \tag{2.10}$$

which generates a measurable transverse magnetization Mx'y', where τ_p is the duration of RF pulse.

After a magnetized spin system has been perturbed from its thermal equilibrium state by an RF pulse with a short duration, it will, according to the laws of thermodynamics, return to equilibrium. The recovery of the longitudinal magnetization M_z is proportional to the difference between the current Mz' and equilibrium longitudinal magnetization M_z^0 before excitation:

$$\frac{dM_{z'}}{dt} = \frac{M_{z'}^0 - M_{z'}}{T_1} \tag{2.11}$$

where T_1 is called the spin-lattice relaxation time, which describes the interaction between spin system and the lattice (the molecular arrangement and structure) of the object. In the transverse plane Mxy, the phase coherence established from the RF pulse is gradually lost due to micro-magnetic field variation, which results in the reduction of the transverse magnetization (T2 relaxation) characterized by:

$$\frac{dM_{x'y'}}{dt} = \frac{-M_{x'y'}}{T_2} \tag{2.12}$$

where $M_{x'y'} = M_{x'}i + M_{y'}j$, T_2 is spin-spine relaxation time which describes the interactions between spins with slightly different precession frequencies. T2 relaxation occurs as a result of dephasing (becoming out of phase) of individual magnetic moments of the protons as they experience a slightly different magnetic field and rotate at a slightly different frequency. T2 relaxation starts immediately after RF pulse application. This transversal relaxation occurs both due to magnetic field inhomogeneities produced by the magnet or by magnetic particles present in the tissues and due to the movement of the molecules in the tissue.

The solutions to the two differential equations are:

$$M_{x'y'} = M_{x'y'}(0)e^{-t/T_2} \tag{2.13}$$

$$M_{z'}(t) = \ M_{z'}e^{-t/T_1} + \ M_z^0(1\text{-}e^{-t/T_1}) \tag{2.14}$$

Therefore, the dynamics of the MR signal in terms of longitudinal and transverse magnetizations can be characterized by exponential equations with respect to relaxation times T_1 and T_2, respectively.

Based on Eqn 2.1, the resonance frequency of a spin system depends on the gyromagnetic ratio and static magnetic field B_0. If B_0 is homogenous, all spins are on resonance and possess the same resonance frequency. In practice, due to macroscopic differences in the static magnetic field (such as nearby iron or gas and their associated electromagnetic fields) even within uniform tissues, protons will precess at very slightly different rates and get out of phase with each other. The dephasing of protons due to these field inhomogeneities causes tissue magnetization to drop off more rapidly than expected from the T2 constant. This dephasing of the transverse magnetization is a combination of two effects: the first related to intra- and inter-molecular magnetic field differences (T2) and the second related to fixed macroscopic field differences due to the presence of different tissues (ΔB). The combination of these intrinsic and extrinsic effects is referred to as T2* and can be expressed using the following formula.

$$\frac{1}{T2^*} = \frac{1}{T2} + \gamma \Delta B \tag{2.15}$$

Thus, the precessing spins may have a range of resonance frequencies due to the off-resonance effects from the aforementioned factors. The spins' resonance frequency in the off-resonance condition is

$$\omega = \ \omega_0 - \ \Delta\omega \tag{2.16}$$

where ω_0 is the Larmor frequency and $\Delta\omega$ is the off-resonance frequency.

The Bloch equation describes the time-dependent change of the magnetization M in the presence of all the above-mentioned phenomena. In the rotational frame of reference, the Bloch equation is given as:

$$\frac{dM_{rot}}{dt} = \gamma M_{rot} \times B_{eff} - \frac{M_{x'y'}}{T_2} + \frac{M_{z'}^0 - M_{z'}}{T_1} \tag{2.17}$$

where B_{eff} is the vector sum of the static magnetic field (B_o) and the additional magnetic field from RF coil.

$$B_{eff} = B_{0,rot}k + B_1^e(t)i = -\frac{\Delta\omega}{\gamma}k + B_1^e(t) \tag{2.18}$$

M_{rot} is the magnetization seen from a rotating frame of reference (rotating at ω_0) that is used to cancel out the effect of B_0 and make our analysis simple.

The solution of the Bloch equation can be derived in two steps. The first step is the RF excitation based on Eqn. 2.7. The second step is to calculate the change of the magnetization due to off-resonance and relaxation when the RF pulse is turned off. More specifically, the solution to the second step is:

$$M_{x'}(t) = e^{\frac{-t}{T_2}}[M_{x'}(0)\cos(\Delta\omega t) + M_{y'}(0)\sin(\Delta\omega t)] \tag{2.19}$$

$$M_{y'}(t) = e^{\frac{-t}{T_2}}[-M_{x'}(0)\sin(\Delta\omega t) + M_{y'}(0)cos(\Delta\omega t)] \tag{2.20}$$

$$M_{z'}(t) = M_{z'}(0)e^{-t/T_1} + M_z^0(1 - e^{-t/T_1}) \tag{2.21}$$

Both steps can be represented by matrix operations. If we define the clock-wise rotational operator about x', y', z' axis, respectively, as

$$R_{x'}(\theta) = \begin{matrix} 1 & 0 & 0 \\ 0 & cos\theta & sin\theta \\ 0 & -sin\theta & cos\theta \end{matrix}$$

$$R_{y'}(\theta) = \begin{matrix} cos\theta & 0 & -sin\theta \\ 0 & 1 & 0 \\ sin\theta & 0 & cos\theta \end{matrix}$$

$$R_{z'}(\theta) = \begin{matrix} \cos\theta & \sin\theta & 0 \\ -\sin\theta & \cos\theta & 0 \\ 0 & 0 & 1 \end{matrix} \tag{2.22}$$

where θ is an arbitrary angle, the excitation from an RF pulse with a flip angle of α and initial phase of φ is then calculated as:

$$M_{rot}^{step1} = R_{z'}(\varphi)R_{x'}(\alpha)R_{z'}(-\varphi)\vec{M}_{\mathrm{rot}}^{0} \tag{2.23}$$

where $R_{z'}(-\varphi)$rotates the rotational frame to a reference frame in which The RF pulse has 0 initial phase and $R_{z'}(\varphi)$ rotates magnetization back to the rotational frame. The second step which involves off-resonance precession and relaxation is given by:

$$M_{rot}^{step2} = E_A R_{z'}(\Delta\omega t)M_{rot}^{step1} + E_B\vec{M}_{rot}^{0} \tag{2.24}$$

where

$$E_A = \begin{matrix} E_2 & 0 & 0 \\ 0 & E_2 & 0 \\ 0 & 0 & E_1 \end{matrix}$$

$$E_B = \begin{matrix} 0 \\ 0 \\ 1 - E_1 \end{matrix}$$

where $E_1 = e^{-t/T_1}$ and $E_2 = e^{-t/T_2}$

Therefore, by combining equations 2.21 and 2.22 the matrix representation of the Bloch equation is

$$\vec{M}_{rot} = E_A R_{z'}(\Delta\omega t)[R_{z'}(\varphi)R_{x'}(\varphi)R_{z'}(-\varphi)\vec{M}_{rot}^{0}] + E_B\vec{M}_{rot}^{0} \tag{2.25}$$

This equation is the basis of the numerical simulation of the Bloch equation.

Chapter 3: Literature Review

3.1 Introduction to MRF

In most clinical procedures involving MRI, weighted images are acquired and a radiologist reads and interprets the images visually. Based on the contrast difference or enhancement patterns anatomical structures are classified as normal and abnormal. This is why MR images are said to be qualitative. This kind of diagnosis based on MRI is prone to error due to the subjectivity of the procedures. Moreover, weighted images are affected by a multitude of factors including physical properties of the tissue, vendor differences in the MR scanners, and differences in the imaging parameters. As a result, the images acquired for the same patient may vary from one center to the other and also from one machine to the other. Images of the same patient may vary from one time to another due to variations in the system parameters used.

MRI has the potential to measure the physical properties of tissues in physical units which could avoid the need for conventional weighted images. Acquiring these properties in physical units is known as quantitative imaging. In the initial stages of development, MRI was hoped to be a quantitative imaging technology. The range of properties that can be imaged with qMRI includes T1, T2, diffusion, perfusion, magnetic susceptibility, and chemical exchange. Using the sensitivity of MRI to these tissue properties, quantitative maps can be generated instead of qualitative anatomical images. In quantitative maps, each pixel in the image represents a value of one specific property of a tissue such as its T1 value.

Because of the inherent time-consuming nature of quantitative images, widespread adoption of qMRI clinically is still, unfortunately, not a reality. Mostly at least two images are needed to be acquired to quantitatively map one tissue property, and each image can potentially take minutes to acquire, and hence it is unpractical to use qMRI. Another reason hindering the adoption of qMRI is that current quantitative methods lack reproducibility. Also, no one tissue property is sufficient alone to answer a complex clinical question. This creates a need to construct multiple maps which require more time.

While it is a challenging endeavor, if adopted clinically, qMRI has several advantages over qualitative imaging. If a tissue changes due to growth, disease, or aging its properties also change. Because abnormalities in a tissue result in a change of its physical properties that are different from healthy tissue, they are identifiable on quantitative maps. By measuring tissue properties qMRI removes the variability of imaging from one vendor to another and also variations due to changes in imaging parameters. qMRI can also be used in longitudinal tracking of a single patient. Serial measurements in a single patient could be compared to determine if an intervention is working. Since quantitative maps represent physical properties of tissues, change in these properties would indicate if a course of treatment is working to restore these properties to normal value. qMRI could also assist in personalized medicine by tailoring treatments to patients. Probability maps for various diseases could be created in the event of an abnormality in a tissue. In addition to identifying anatomical abnormalities, qMRI can be used to identify loss of function to assist in fields such as endocrinology. Since maps from different measurements (institutions and vendors) will be consistent, they can be used for Artificial Intelligence (AI) based analysis which requires consistent data.

Current advancements in hardware and computing, parallel imaging, sparsity-based construction algorithms, storage, and AI are making quantitative methods close to reality. In the future, MRI scanners would be more and more quantitative and will provide quantitative and reproducible property maps identifying tissue health.

The concept of traditional quantitative techniques developed so far is the same. The equilibrium magnetization is excited using a radiofrequency pulse and the exponential decay to equilibrium is observed. Most T1 quantification are based on free induction decay signal of saturation recovery using Eqn 3.1

$$M(x,y) = M_0(1 - e^{\frac{-TR}{T_1}})e^{-\frac{TE}{T_2}} \tag{3.1}$$

The T2 effect is made negligible by setting the echo time$(TE) \ll T2$. Saturation recovery measures two or more points along the exponential curve with varying TR. Then uses least square curve fitting to fit the data. This method is sensitive to imperfect FA. To avoid B_o inhomogeneity effects, spin-echo sequences are commonly used for T2 measurements. Using the freed induction decay signal in the above equation, T2 is measured with varying echo times TE. Then least square curve fitting is used to fit the data. To reduce the effect of T1 in these measurements, we make TR >> T_1.

To reduce the acquisition time of quantitative maps, several techniques have been proposed. Most of the methods try to reduce scan time by improving sampling through the use of non-cartesian sampling, EPI, and parallel imaging. In most methods, T1 and T2 are determined using two separate experiments. Various techniques for shortening the acquisition time of qMRI methods have been developed [33, 34, 35]. Methods to quantify multiple parameters simultaneously are also proposed [36]. All of these methods utilize fixed flip angles to acquire the signal along the exponential curve. As the T1 and T2 relaxation curves are exponential in nature, the accuracy of estimating these parameters could be affected by signal variation due to motion and undersampling artifacts.

3.2 Principles of Magnetic Resonance Fingerprinting

To overcome the shortcomings of current quantitative methods in MRI, magnetic resonance fingerprinting (MRF) was proposed with a novel approach to the whole process of acquiring maps of the physical properties of tissues. MRF enables the quantification of multiple properties like T1, T2, and PD in a single experiment in a time comparable to that is needed to acquire one property by other methods.

The fundamental premise of the MRF concept is that, with the use of a suitable acquisition strategy, distinct signal evolutions (fingerprints) can be produced for various materials or tissues with various underlying properties. As its name suggests, MRF is inspired by the way real human fingerprints work. In the identification of humans based on fingerprints, there are three main steps. First, a database of fingerprints of all of the population in a certain group is recorded and stored along with the information about each individual (like name and address) to create a dictionary of all fingerprints. When there is a need to identify a certain individual, his/her fingerprint is scanned. During the pattern recognition step, the recorded fingerprint of the individual is compared (matched) against all the atoms (entries) in the prerecorded database (dictionary). Based on a presetted similarity criterion, the atom from the dictionary that produced the highest match score is selected as the best match and information about the person is retrieved. Likewise, MRF contains the same three steps (dictionary generation, signal acquisition, and pattern recognition) to identify tissues in the human body. As conventional fingerprint-based identification requires each human to have unique fingerprints, MRF requires different signal evolution from tissues with different properties. The requirement of uniqueness can be fulfilled by using a pulse sequence (acquisition scheme) that is sensitive to those properties.

In the dictionary generation stage, the signal evolution of all the tissues (fingerprints) in a specific region of the body (with all possible combinations of tissue properties) is recorded by applying a carefully designed acquisition scheme (pulse sequence) and the signal evolution for each combination of properties is stored together with the values of the properties used to generate the signal. Then when a patient comes for diagnosis, the same pulse sequence is applied to acquire a series of undersampled images as the signal evolves and the signal evolution for each area (voxel) in the organ being imaged is acquired. Finally, pixel-wise pattern matching is done with each dictionary entry and the best match is chosen. Based on the match, the physical properties of that voxel (representing a certain tissue) are retrieved from the dictionary and portrayed as pixel-wise maps that are perfectly registered to one another, hence delivering quantitative and structural information [37] (see Fig. 3.1). This procedure is repeated for each voxel in the object being imaged.

The first work on MRF by Ma et al. [10] measure the properties T1, T2, and B0 inhomogeneity. Researchers later studied other properties including radio frequency transmitter field inhomogeneity (B1 inhomogeneity) [38, 39], T2* [40], and perfusion [41].

Unlike conventional MRI techniques which acquire a steady state signal with constant parameters, by varying the acquisition parameters in the sequence, MRF keeps the signal in a transient state and constantly acquires new information in each sampling. This way, MRF achieves temporal and spatial variations between each pixel. Also, acquisition in a transient state eliminates the time needed to reach a steady state. Because of the robustness of the matching methods, MRF is less prone to errors induced by motion and undersampling. Although MRF-based acquisitions can be relatively robust to motion effects occurring at the beginning or end of the sequence, relying on redundancy in the data alone is not sufficient to assure the accuracy of the multi-parametric maps in all cases.

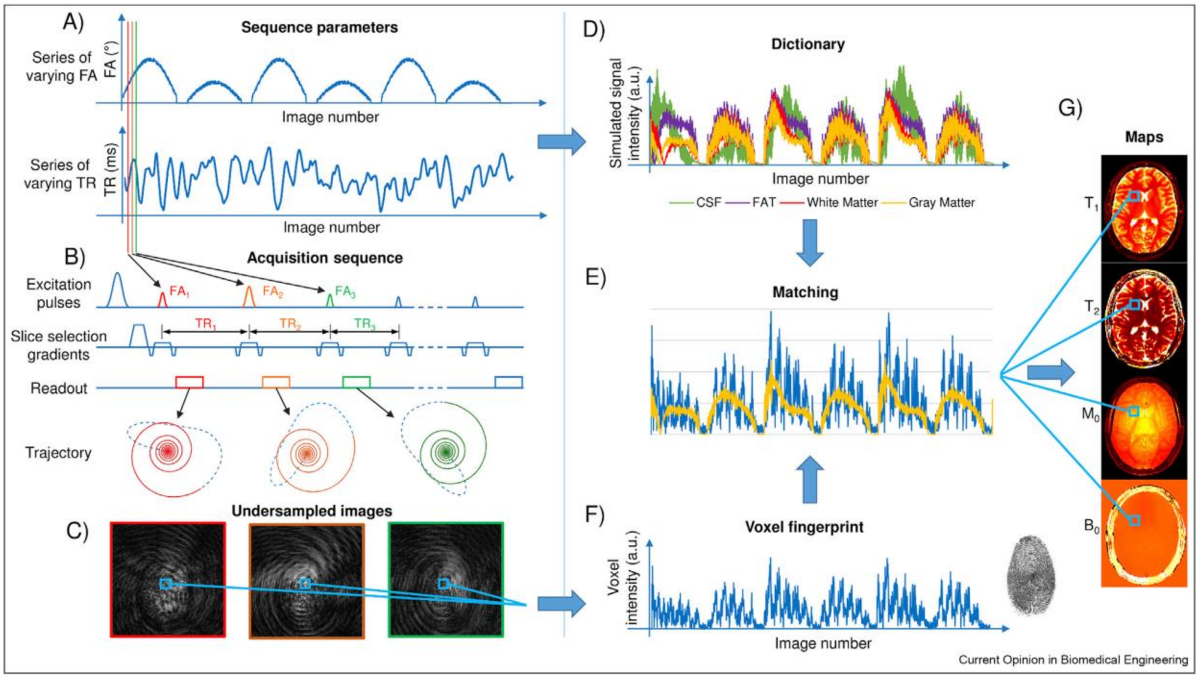

Figure 3. 1: *Flowchart for 3D MRF: A) Variable flip angles (FA) and repetition time (TR) used for dictionary generation and image acquisition, (B) Sequence diagram of True Fast Imaging with Steady State Precession (TruFISP) displaying the readout gradients, k-space trajectory, slice selection gradients, and excitation pulses for each TR, (C) Three of a series of highly undersampled images acquired at different TR, (D) Four dictionary atoms representing the four major brain tissues: white matter (T1 = 850 ms, T2 = 50 ms), gray matter (T1 = 1300 ms, T2 = 85 ms), fat (T1 = 400 ms, T2 = 53 ms), and cerebrospinal fluid (CSF) (T1 = 5000 ms, T2 = 500 ms), (E) Demonstrates how to extract the tissue properties that are represented by that voxel by pattern matching the fingerprint of that voxel with the nearest entry in the dictionary, (F) Example tissue fingerprint showing intensity variations across the undersampled images, (G) Displays parameter maps that were created by going through the matching procedure for all voxels [37].*

3.2.1 Pulse sequence design

The robustness of MRF pattern matching offers great flexibility in designing pulse sequences. In MRF, the focus is on producing unique signal evolutions that are spatially and temporally incoherent for each voxel so that they can be uniquely identified by a pattern-matching algorithm. Thus, the pulse sequence or acquisition parameters like FA and TR can be varied as long as they meet uniqueness requirements. Hence, careful design is necessary to obtain useful information. The pulse sequence also determines the relevant combination of tissue properties that can be measured as well as how time-efficient, accurate and precise the experiment is. Because of this, almost all pulse sequences can be adapted for MRF experiments.

The original work on MRF was based on the inversion recovery balanced steady-state free precession (IR-bSSFP) sequence [10]. This sequence was chosen because it is known to be sensitive to T1, T2, and off-resonance frequencies. Later works used other sequences to eliminate banding artifacts in bSSFP sequences and measure other tissue properties like $T2^*$.

3.2.2 Dictionary generation

To generate the dictionary, we first identify our properties of interest; then values in the feasible physiological range of each property are selected. After that, a pulse sequence is designed that is sensitive to the properties of choice. Once the pulse sequence is designed, a simulation is done to generate a signal evolution for each combination of property values. There are two common ways employed to simulate a dictionary of feasible signal evolutions. The first method is based on Bloch simulation which was used in the original work [10] and the other method is using the extended phase graph formalism [42]. There are also other more complex techniques used to generate databases of expected signal evolutions in a shorter time. For each new sequence, a dictionary of signal evolutions is generated on a computer using one of the simulation techniques.

3.2.3 Data acquisition

In conventional MRI, the same acquisition parameters (FA, TR, and k-space trajectory) are repeated in a particular sequence until sufficient k-space samples are acquired. Because of this, the image will be weighted by a particular property. The effect of other properties is reduced by meticulous design.

To achieve the key assumption of temporal and spatial incoherence between signal evolutions of different voxels, MRF continuously varies the acquisition parameters throughout the data collection. MRF acquires a series of undersampled images by using different parameters for each image. Because the parameters are varying, the signal will not reach a steady state and remains in a transient state. Hence, by sampling the transient signal, MRF keeps on acquiring new information and each image makes the signal evolution for each voxel more unique. The number of images acquired depends on the accuracy of the method used in resolving the signal evolutions. In the original work on MRF [10], a series of 1000 undersampled images were acquired. By using improved matching algorithms, other works reduced the number of images required for uniqueness [43].

Acquisition time reduction is critical for volumetric coverage and coverage of large body regions. To reduce the time, two main techniques can be employed: reduce the acquisition time of each image in the series and/or reduce the number of images acquired. To reduce the acquisition time of individual images, the number of samples acquired for reconstruction can be reduced. This can be achieved by using different k-space trajectories like spiral, radial, and echo-planar imaging. However, this will produce undersampling artifacts in the images from each time point. Each trajectory is re-ordered at each experiment to further reduce signal coherence between voxels. Depending on the experimental parameters, the re-ordering can be sequential, uniformly rotated, or random. Sequential re-ordering with spiral trajectory was utilized by Ma, et al. [10] for bSSFP based sequence.

Contrary to conventional mapping methods, the artifacts in each image are unimportant as long as they do not interfere with the pattern-matching procedure because the emphasis is entirely on creating quantitative maps of interest. As a result, high-quality individual time point images are not specifically desired. Despite substantial undersampling, the signal evolution produced from all undersampled data can still be matched to the most related MRF dictionary entry, and the quantitative maps produced have been proven to be highly accurate [37]. As a result, since the undersampling errors are not coherent in space or time, it is feasible to “see through” image artifacts caused by undersampling during the dictionary-matching process. Alternatively, we reduce the number of acquired images and use an improved pattern-matching algorithm like iterative reconstruction or AI-based reconstruction. Through the use of simultaneous multislice imaging techniques, scan times have also been shortened**.**

3.2.4 Pattern recognition and quantitative map visualization

Before the pattern matching step commences, a signal evolution vector (fingerprint) for each voxel (resenting a tissue voxel) is constructed by selecting all the intensity values at the pixel’s location from all of the acquired series of undersampled images (F in Fig. 3.1). Then a pattern match between a voxel’s signal evolution and the overall dictionary of possible signal evolutions generated for that sequence is done. By using suitable metrics, a dictionary atom that best matched the pixel is selected as a match and sorted. Then the values used to generate the signal evolution of the matched dictionary atom are retrieved from the database and assigned to the voxel’s location in the respective maps of tissue properties. This process is repeated for all pixels. Finally, property maps are visualized.

Different pattern-matching algorithms have been proposed in the literature. In [10] template matching based on the dot-product between the acquired signal and each simulated fingerprint signal is used. The T1, T2, and B0 values used to create the dictionary entry that had the highest dot product were allocated to that voxel as the best match. The PD is computed as the ratio of the acquired signal evolution and the matched dictionary entry. Since the dictionary is constructed assuming a PD of one, any additional magnitude is assumed to come from the extra PD. This matching algorithm took approximately two and half minutes for two-dimensional brain imaging on a standard desktop computer.

Other methods of pattern matching have been proposed. McGivney et al. used singular value decomposition (SVD) to compress the dictionary in the time domain and speed up the matching by a factor of 3.4 – 4.8 [44]. Other studies employed an iterative reconstruction algorithm to address large-size MRF problems encoding a large number of properties such as $T2^*$, perfusion, diffusion, microvascular properties, etc [45, 46]. Methods using machine learning for MRF reconstruction have also been proposed [47, 48, 49, 50].

3.3 Related Works

The pioneering study by Ma et al. [10] utilized the IR-bSSFP sequence, randomized flip angle and repetition times, and spiral undersampling in k-space to precisely map T1, T2, off-resonance frequency, and proton density of the human brain. Their study showed that MRF exhibits an efficiency approximately 1.8 times higher than the previously favored DESPOT methods, which were considered the most efficient techniques for relaxation time measurements.

While the bSSFP signal is sensitive to both T1 and T2, the presence of banding artifacts arising from inhomogeneous fields can still impact the accuracy of quantification. To address this limitation, Jiang et al. [51] introduced the application of fast imaging with steady-state precession (FISP) sequence, which enables the acquisition of coherent steady-state signals with a constant unbalanced gradient moment in each repetition time. By employing this approach, they successfully achieved precise quantification of T1 and T2. Using the FISP sequence eliminates the need to consider off-resonance effects, resulting in a smaller dictionary size compared to bSSFP when considering the same T1 and T2 resolution. Consequently, this leads to faster calculation times for the pattern-matching algorithm or the possibility of enhancing dictionary resolutions for T1 and T2 values.

To expedite the pattern-matching step within the MRF framework, McGivney et al. [52] proposed to compress the dictionary using SVD, thereby achieving a low-rank approximation. By reducing the size of the dictionary in the time domain, they were able to accelerate the pattern recognition algorithm, which relies on the dot product between the dictionary and the signal evolution of each pixel. This compression technique resulted in a speed improvement ranging from 3.4 to 4.8 times faster, while still maintaining the high signal-to-noise ratio of the original scheme introduced by Ma et al. [10].

Another significant development in the MRF framework is the work by Davies et al. [45] which proposed an iterative reconstruction algorithm based on compressed sensing. By employing iterative reconstruction algorithms, they achieved precise quantification using a reduced number of excitation pulses—only 200, compared to the previous works which used1000 repetitions. As a result, they were able to achieve accurate recovery of the proton density, T1, T2, and off-resonance maps simultaneously from a limited number of samples.

As the number of parameters to be quantified increases, the pattern matching algorithm becomes slower due to the growing size and complexity of the fingerprint dictionaries in multi-parametric quantitative MRI applications. Golbabaee et al. [46] addressed this limitation by arranging dictionary atoms in the form of cover tree structures and adopting the corresponding fast approximate nearest neighbor searches to accelerate matched filtering. To address large-scale MRF problems involving multiple intrinsic NMR parameters, they proposed an iterative reconstruction algorithm called CoverBLIP. The authors demonstrated that, by incorporating the concept of embedding, the inexact and non-convex iterations of CoverBLIP exhibited linear convergence towards a near-global solution with accuracy comparable to that achieved through exact brute-force searches. Through the utilization of synthetic and real-world datasets, along with various sampling strategies, they achieved a reduction in total search computations, ranging from two to three orders of magnitude.

Optimization of the sampling trajectory in MRF is still an open problem. In MRF data sampling, spiral [10, 51] and radial [53, 54] trajectories are often used as they have higher spatial incoherence and sampling efficiency. However, echo-planar imaging (EPI) and Cartesian trajectories [55, 56] have also been shown to be useful in the MRF framework. The optimization of the trajectory in MRF remains an ongoing challenge. In a recent study, an analytical model has been proposed to address this issue by incorporating the effects of both sequence design and k-space sampling [57].

3.4 Applications of MRF

MRF has so far primarily been employed in clinical trials for the prostate and the brain, but it has also shown promise in applications for the heart, musculoskeletal system, and the abdomen. In 56 healthy participants, Badve et al. [58] simultaneously estimated T1 and T2 relaxometry values for several brain areas using the MRF framework. MRF-derived T1 and T2 values were utilized in research on 31 patients with intra-axial brain lesions to distinguish between gliomas and metastases [59]. Yu et al. showed the viability of using an exam that combined MRF-SSFP and apparent diffusion coefficient (ADC) mapping to distinguish between cancer and healthy prostate in the peripheral zone of the prostate [60]. Using a breath-hold acquisition of 16 heartbeats, cardiac MRF, as described by Hamilton et al. [61], allowed simultaneous estimation of T1, T2, and M0 values. Christen et al. [62] used MRF to quantify microvascular parameters such as cerebral blood volume (CBV), mean vessel radius (R), and blood oxygenation saturation (SO2).

Chapter 4: Methodology

4.1 Pulse Sequence

The long TR needed to allow the transverse and longitudinal magnetization to fully decay and recover respectively, is one factor in the time-consuming nature of MR acquisitions. SSFP sequence uses short TR to establish a dynamic equilibrium state with a high signal-to-noise ratio (SNR) to allow fast imaging. In this thesis, IR-bSSFP pulse sequence as shown in Fig. 4.1 has been utilized. The term balanced refers to the fact that the summation of the gradients in each encoding direction is zero. bSSFP is known to be sensitive to changes in T1, T2, and off-resonance frequencies. An inversion pulse is added at the beginning of the sequence to increase T1 sensitivity.

The sequence uses flip angles of repeating sinusoids with a length of 250 TRs. The flip angle was determined for the odd periods using the formula $FA_t = 10 + \sin\left(\frac{2\pi}{500}t\right) * 50 + random(5)$, where $1 \leq t \leq 250$ and $random(5)$ is a random number uniformly distributed between 0 and 5. The flip angle from the prior period was divided by 2 for the even periods. To allow for differential signal decay according to T2 and differential magnetization recovery according to T1, a 800ms delay of 0^0 flip angles was inserted between each of the periods as shown in Fig. 4.2. The TR is a constant 16ms. The phase of the RF pulses alternates between 0 and 180°. A matrix size of 256 x 256 x 1 and a field of view (FOV) of 30cm was assumed [10].

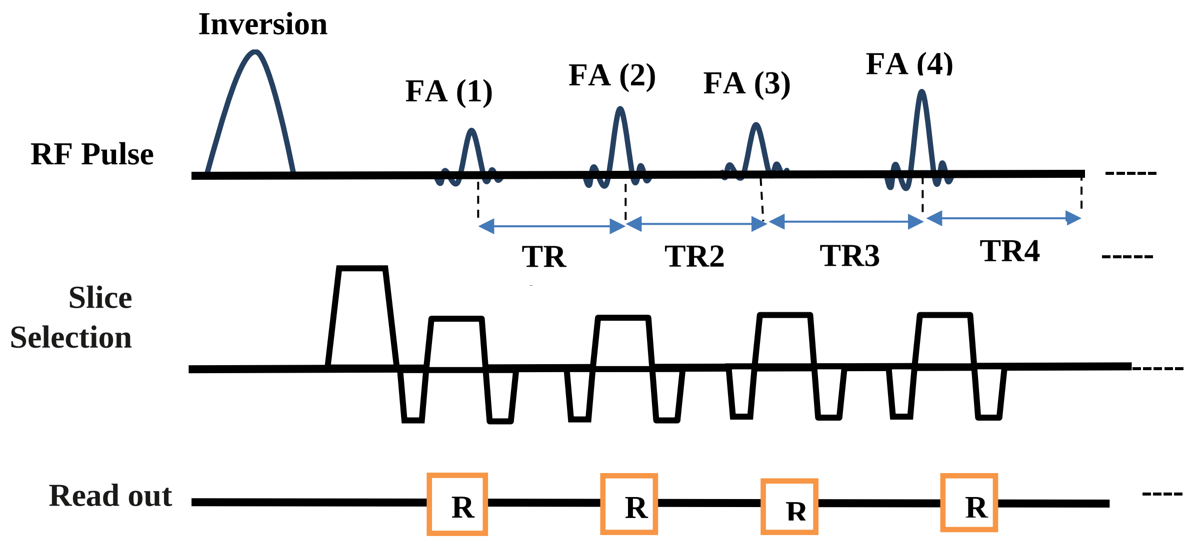

Figure 4. 1*: Acquisition sequence diagram*

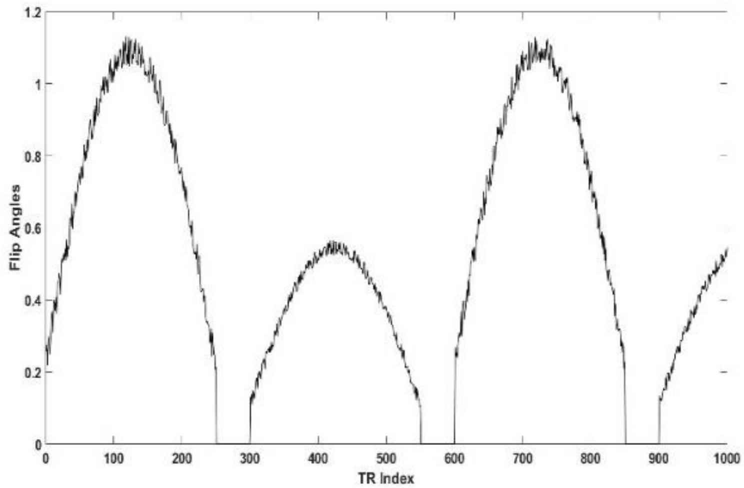

Figure 4. 2*: RF pulses*

4.2 Dictionary Generation

A dictionary of expected signal evolutions was built through Bloch simulation using MATLAB software on a personal computer with a 2.2 GH CPU and 16 GB RAM. The focus of this thesis is characterizing the parameters T1, T2, and off-resonance frequencies. A dictionary of expected signal evolutions within the physiological range of T_1 , T_2 , and off-resonances frequencies (excluding the unrealistic scenarios of combinations of T1 and T2 values where T2 is greater than T1 values) was simulated and stored for later stages. The resolution of the dictionary is as stated in a previous study [10].

The range of values simulated are 100ms to 5000ms for T1, 20ms to 3000ms for T2, and -400Hz to 400Hz for off-resonance frequencies. Tables 4.1, 4.2, and 4.3 show the resolution of the values used for T1, T2 and off-resonance respectively.

T1 Resolution (ms)	**Range (ms)**
20	T1 < 2000
300	T1 > 2000

Table 4. 1*: The range and resolution of T1 values simulated in the dictionary*

T2 Resolution (ms)	**Range (ms)**
5	T2< 100

10	100< T2 < 200
200	T2 > 200

Table 4. 2: *The range and resolution of T2 values simulated in the dictionary*

Off-resonance Resolution (Hz)	**Range (Hz)**
1	-40 to 40
2	-80 to -42 and 42 to 80
10	-250 to -90 and 90 to 250
20	-400 to -270 and 270 to 400

Table 4. 3*: The range and resolution of off-resonance values simulated in the dictionary*

4.3 K-space Trajectory Design

In this thesis two ways of sampling k-space were utilized. First one was based on spiral sampling and the second was based on EPI. In both designs, at the end of each readout, the zero order gradient moments for Gx and Gy were nulled so that stationary spins will not contribute to the MR signal phase.

4.3.1 Spiral trajectory design

To ensure the undersampling capability of MRF sequences, variable density spiral trajectory was used during data acquisition. This trajectory oversamples the inner k-space, so that central part of the inner k-space remains fully sampled. Since most of the energy of an image is concentrated near the k-space origin, it is desirable to accurately resolve the signals at low spatial frequencies than signals at higher spatial frequencies.

The sampling density is proportional to the FOV. Which implies, with variable-density sampling, the FOV becomes a variable. It should be noted that this effective (variable) FOV is different from the nominal FOV that defines the FOV of interest, which has a constant value. There are several methods that can be used to design the spiral trajectory in the Kx–Ky plane. In the current work, a method that uses fixed limits on the gradient amplitudes and slew rate is used. The constraints involved in designing the spiral trajectories are as follows: First, hardware constraints limit the maximum gradient amplitude and slew rate. Since the starting angle of the trajectory is a variable for interleaved spiral imaging, the gradient vector magnitude and slew rate vector magnitude are constrained. Second, FOV requirements place a limit on the rate of increase in the radial direction compared with the rate of turning. The FOV also places a limit on the maximum gradient vector magnitude.

The desired Archimedean spiral trajectory can be described as

$$K = K_r e^{i\theta} \tag{4.1}$$

where

$$K = K_x + iK_y, \qquad K_r = \sqrt{{K_x}^2 + {K_y}^2}, \quad \theta = atan\frac{K_y}{K_x} \tag{4.2}$$

A variable density spiral trajectory, which fully samples the k-space with 24 interleaves is designed. Only one of the 24 interleaves is used in acquisition of each time series image and hence a 24-fold undersampling of the Fourier space (k-space) is achieved. The spiral shots in the MRF pulse sequence are repeated by incrementing the rotation angle by 15° to fill the *k*-space. The designed trajectory is shown in Fig. 4.3.

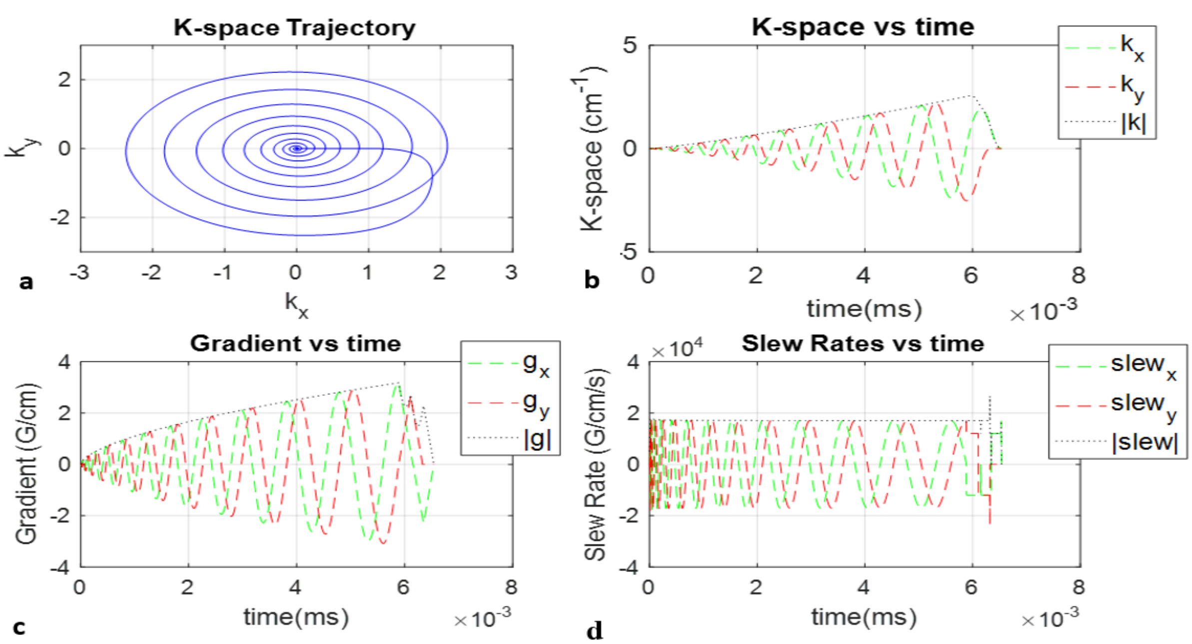

Figure 4. 3*: Spiral trajectory design: (a) k-space trajectory (b) k-space location versus time (c) the gradient versus time (d) the slew rate versus time*

4.3.2 Multi-shot echo-planar imaging trajectory design

For this trajectory, an acquisition scheme similar to [19] is used as shown in Fig. 4.4. This method is based on a cartesian grid Fourier sub-sampling, where 16 out of 256 lines from the k-space (with uniform spacing) are simultaneously sampled at each repetition time. The sixteen-shot sampling pattern will be moved by one line in the following time frame, and so on. This results in a data that is undersampled sixteen-fold which results in significant undersampling artifacts.

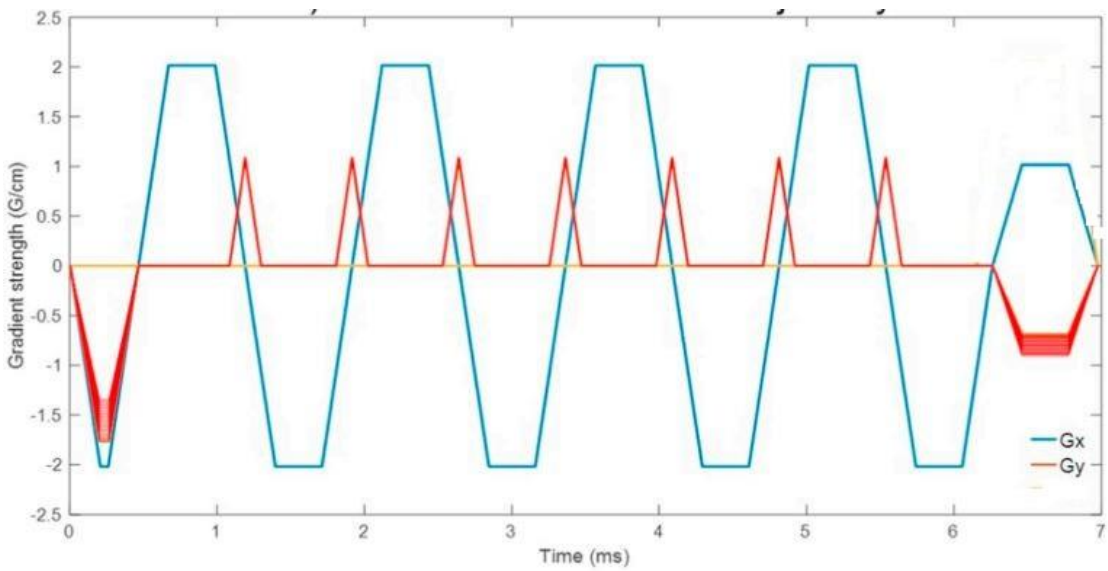

Figure 4. 4: *Gradients designed for echo-planar imaging [19]*

4.3.2.1 Readout Gradient (Gx)

The readout gradient waveform in EPI starts with a prephasing (dephasing) gradient lob followed by a series of readout gradient lobs with alternating polarity. Fig 4.5 shows detailed design of the readout gradient. It shows the design for the dephasing and the first readout gradient design. For the next readout, the readout gradient is multiplied by -1.

In Fig. 4.5, t_f is the dephasing time, t_s is sampling time and G_{xMax} is maximum readout gradient amplitude. For a field of view FOV and bandwidth BW, the maximum readout gradient is calculated from the Nyquist criterion as:

$$G_{xMax} = \frac{1}{(\gamma\left(\frac{1}{Bw}\right)FOV)} \tag{4.3}$$

where BW is equivalent to the inverse of the time between samples (dwell time, *dt*).

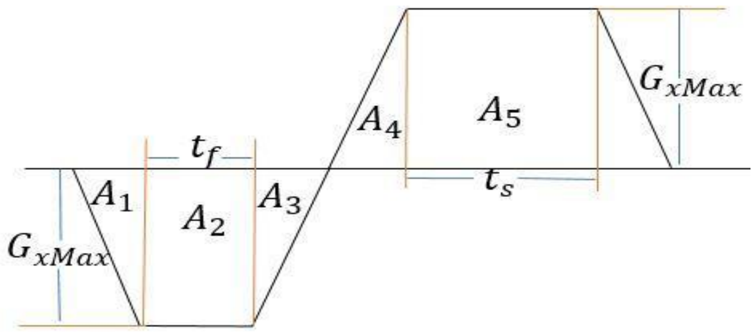

Figure 4. 5*: Readout gradient design*

The sampling time for a single k-space line is

$$t_s = N_x\left(\frac{1}{BW}\right) = N_x(dt) \tag{4.4}$$

where N_x is the number of samples in the x-direction.

The slew rate (SR) in MRI is defined as the speed at which the gradient reaches its maximum amplitude. If we define "rise time" t_r as the time taken by G_x to reach G_{xMax} from a value of 0, we have

$$SR = \frac{G_{xMax}}{t_r} \text{ and } t_r = \frac{G_{xMax}}{SR}$$

From Fig. 4.4 the areas of the triangles and rectangles are given by

$$A_1 = \frac{1}{2}\, t_r G_{xMax} = \frac{1}{2}\frac{G_{xMax}{}^2}{SR} \tag{4.5}$$

$$A_2 = t_f G_{xMax} \tag{4.6}$$

$$A_5 = t_s G_{xMax} \tag{4.7}$$

Since $A_3 = A_4$, $A_1 + A_2$ should be equal to half of A_5, where A is area.

$$\frac{1}{2}\, t_r G_{xMax} + t_f G_{xMax} = \frac{1}{2}\, t_s G_{xMax} \tag{4.8}$$

which gives us

$$t_f = \frac{1}{2}(t_s - t_r) = \frac{1}{2}\left(t_s - \frac{G_{xMax}}{SR}\right) \tag{4.9}$$

Eqn. 4.9 gives us the time we need to apply the dephasing gradient.

4.3.2.2 Phase encoding Gradient (Gy)

The phase encoding gradient in EPI starts with a prephasing (dephasing) gradient followed by a series of small triangular gradient lobs (Blips) that are used to jump from one k-space line to the next with area proportional to the inverse of the FOV (Fig 4.6).

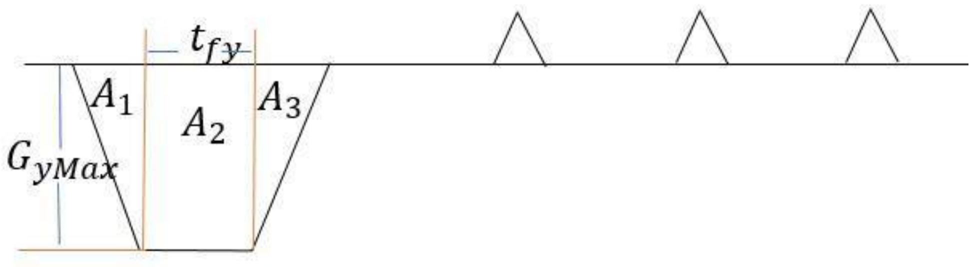

Figure 4. 6: *Phase encoding gradient design for EPI*

The total area under the dephasing gradient lob (A_1+A_2+A_3) in Fig 4.5 is proportional to the maximum frequency we want to achieve in the y (phase encoding) direction and

$$A_T = A_1 + A_2 + A_3 = \frac{k_{yMax}}{\gamma} \tag{4.10}$$

$$\frac{1}{2}G_{yMax}\left(\frac{G_{yMax}}{SR}\right) + t_{fy}G_{yMax} + \frac{1}{2}G_{yMax}\left(\frac{G_{yMax}}{SR}\right) = \frac{k_{yMax}}{\gamma} \tag{4.11}$$

$$\frac{{G_{yMax}}^2}{SR} + t_{fy}G_{yMax} - \frac{k_{yMax}}{\gamma} = 0 \tag{4.12}$$

$${G_{yMax}}^2 + (SR)t_{fy}G_{yMax} - \frac{(SR)k_{yMax}}{\gamma} = 0 \tag{4.13}$$

$$G_{yMax} = \frac{-(SR)t_{fy} + \sqrt{((SR)t_{fy})^2 + 4\left(\frac{(SR)k_{yMax}}{\gamma}\right)}}{2} \tag{4.14}$$

Blip gradient lob

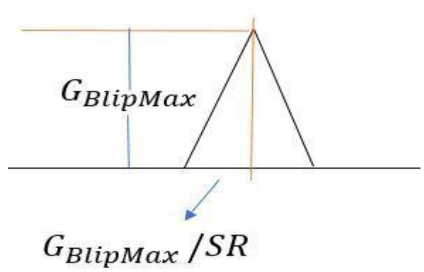

Figure 4. 7: *Blip lob design*

The area under the blip gradient lob is proportional to the jump in k-space in the y direction.

Thus from Fig. 4.7,

$$A_{BliP} = 2(\frac{1}{2}(G_{BlipMax}/SR)G_{BlipMax}) \tag{4.15}$$

$$2(\frac{1}{2}(G_{BlipMax}/SR)G_{BlipMax}) = \frac{nShot\Delta k}{\gamma} \tag{4.16}$$

where *nShot* is the number of shots (16 in our case) and Δk the distance between two k-space lines.

$$\frac{{G_{BlipMax}}^2}{SR} = \frac{nShot\Delta k}{\gamma} \tag{4.17}$$

$$G_{BlipMax} = \sqrt{\frac{nShot\Delta k}{\gamma}(SR)} \tag{4.18}$$

The resulting trajectory in k-space can be seen in Fig 4.8.

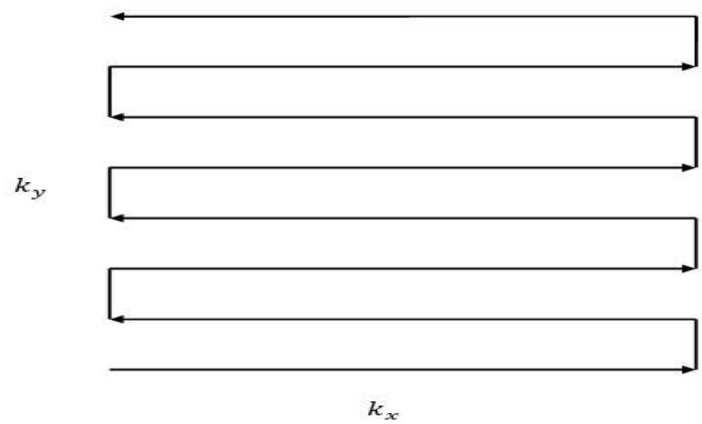

Figure 4. 8: *K-space trajectory for multi-shot EPI. In each shot only 16 out of the 256 lines in k-space are acquired*

4.4 Bloch Simulation of MRF

The general block diagram of the framework used for simulating the whole MRF method is shown Fig. 4.9. A similar framework has been used previously in [63]. Numerical phantoms, pulse sequence and the sampling trajectory are given as inputs to the Bloch simulator. The simulator outputs a series of undersampled images. Sampled images are reconstructed using the Fast Fourier Transform in MATLAB for echo-planar imaging. For spiral sampling, the reconstruction is performed using the non-uniform Fast Fourier Transform (NUFFT) algorithm [64]. Next, signal evolutions for each pixel are built by taking the value of the pixel from all series images. Then a pattern matching step finds best match for each pixel from the dictionary and stores the index of the entry with the best match. Using this index, quantitative map is constructed for each property and visualized.

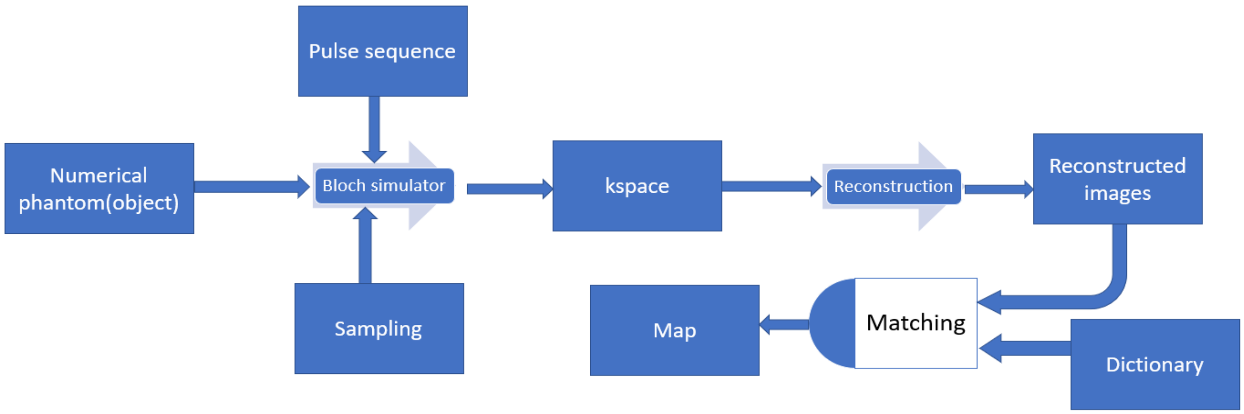

Figure 4. 9: Block diagram of the simulator

4.5 Data Acquisition

In this step, a set of baseline images (1000) are acquired by pseudorandomly varying the acquisition parameters (FA, TR and trajectory) as described in section 4.1.

4.6 Numerical Phantoms Design

In order to test the performance of the two sampling techniques, two kinds of numerical phantoms were used: cylindrical phantoms and simulated brain database phantoms [65, 46].

4.6.1 Cylindrical numerical phantoms

The MATLAB function "phantom" which generates segments of elliptical shapes was used in this process. The function accepts the additive intensity value of the ellipses, the length of the horizontal and vertical semi-axis of the ellipses, x and y coordinates of the center of the ellipses and the angle between the horizontal semi-axis of the ellipses and the x-axis of the image.

A numerical phantom with six ellipses which are representative of the six main tissues in brain (CSF, grey matter, white matter, fat, muscle and skin) was generated. These six regions were used to generate T1, T2, off resonance and PD phantoms which serve as ground truth maps. We assigned specific T1, T2, off resonance, and proton density values to each region based on existing tables from basics of MRI web book as shown in Table 4.4.

Tissue	T1(ms)	T2(ms)	Off-resonance frequency (Hz)	Proton density	Phantom index
Background	0	0	0	0	0
CSF	5012	512	-20	100	1

Gray matter	1545	83	-40	100	2
White matter	811	77	-30	80	3
Fat	530	77	50	80	4
Muscle/skin	1425	41	250	80	5/6

Table 4. 4: *T1, T2, off-resonance, and proton density values assigned to the six regions of the cylindrical phantoms*

4.6.2 Brain numerical phantoms

Another numerical phantom used is from BrainWeb MNI simulated Brain databases as used in [46]. It contains simulated brain MRI data based on two anatomical models: normal and multiple sclerosis. The normal phantom is used in the current work. The MNI brain phantom is segmented into nine regions (0=Background, 1=CSF, 2=Grey Matter, 3=White Matter, 4=Fat, 5=Muscle/Skin, 6=Skin, 7=Skull, 8=Glial Matter, 9=Connective tissue). It has size of 217x181x181. In order to simulate 2D acquisition, only one slice is selected and assigned T1, T2 and PD values to each segment. The Glial Matter and connective tissues were set as background. The values used for each region can be seen in Table 4.5.

Tissue	**T1(ms)**	**T2(ms)**	**Off-resonance frequency (Hz)**	**Proton density**	**Phantom index**
Background	0	0	0	0	0
CSF	5012	512	-20	100	1
Gray matter	1545	83	-40	100	2
White matter	811	77	-30	80	3
Fat	530	77	50	80	4
Muscle/Skin	1425	41	250	80	5/6

Table 4. 5: *T1, T2, off-resonance, and proton density values assigned to the six regions in brain phantom*

4.7 Pattern Recognition

Although there are various pattern recognition algorithms utilizing sparsity of the signal, a simple template matching using dot product has been implemented in the current work as also described in [10]. For each pixel, the dot product between the signal evolution of the pixel and each dictionary entry was computed and the entry that resulted with maximum dot product was selected as the best match for that pixel. The same process is repeated for each pixel and the property maps for T1, T2 and off resonance are generated.

Chapter 5: Results and Discussions

5.1 Dictionary of Signal Evolutions

A total of 314,160 dictionary entries, each with 1000 time points, were generated. A look up table holding combination of property values was built in order to retrieve the values after a match is found. Figure 5.1 shows normalized dictionary entries generated using the pulse sequence shown in section 4.1.

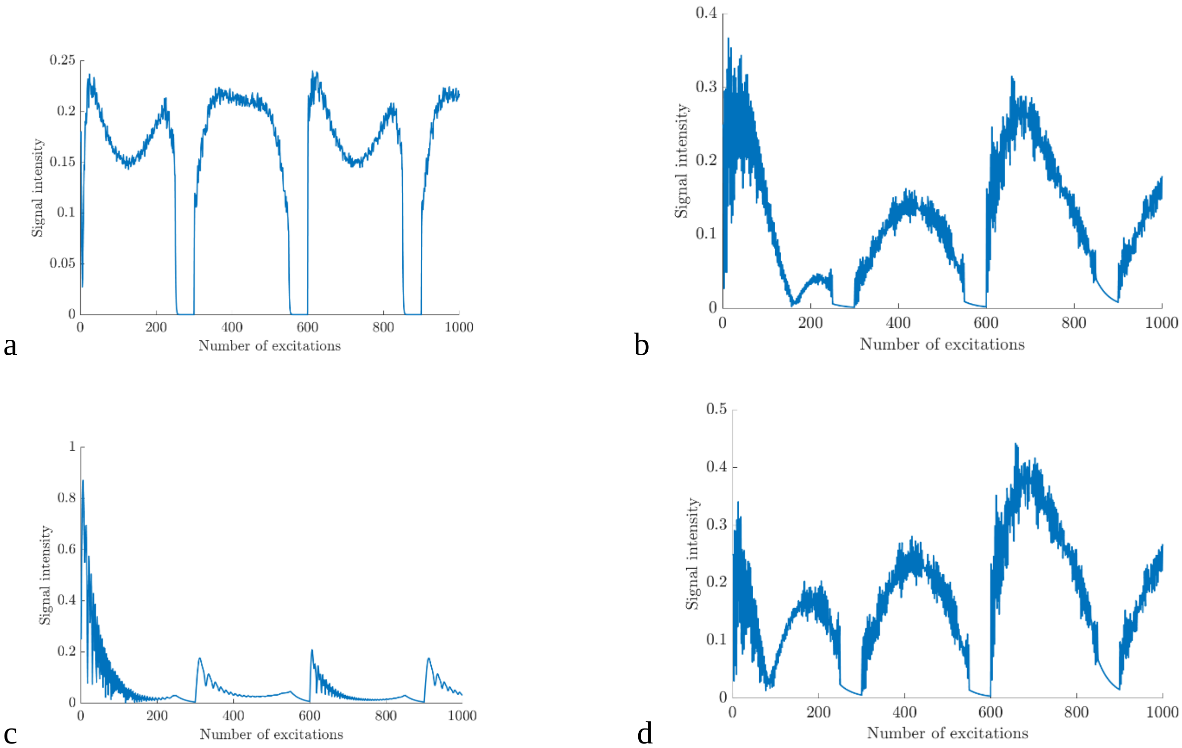

Figure 5. 1: *Sample entries (atoms) in the dictionary with normalized intensity values: (a) T1 = 100ms, T2 = 20ms, off resonance frequency = -40Hz; (b) T1 = 5000ms, T2 = 500ms, off resonance frequency = -10Hz; (c) T1 = 4106ms, T2 = 412ms, off resonance frequency = -30Hz; (d) T1 = 1986ms, T2 = 526ms, off resonance = 240Hz*

5.2 Numerical Phantoms Generation

5.2.1 Cylindrical numerical phantoms

Figure 5.2 shows the cylindrical phantoms generated as described in section 4.6.1.

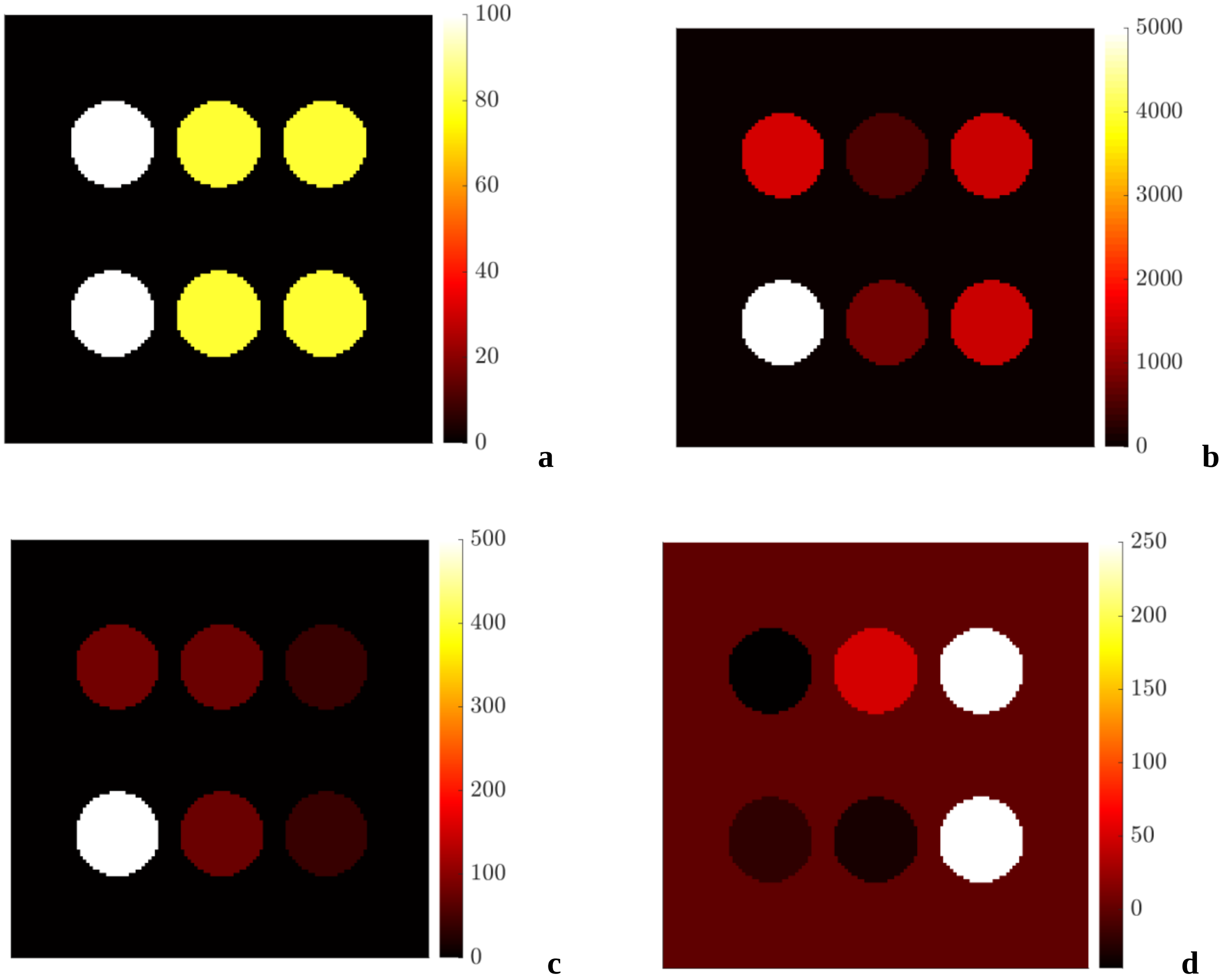

Figure 5. 2: *Ground truth cylindrical phantoms used in the experiment: (a) proton density, (b) T1 phantom(ms), (c) T2 phantom(ms), (d) off-resonance(Hz)*

5.2.2 Brain numerical phantoms

Figure 5.3 shows the brain phantoms generated in MATLAB as described in section 4.6.2

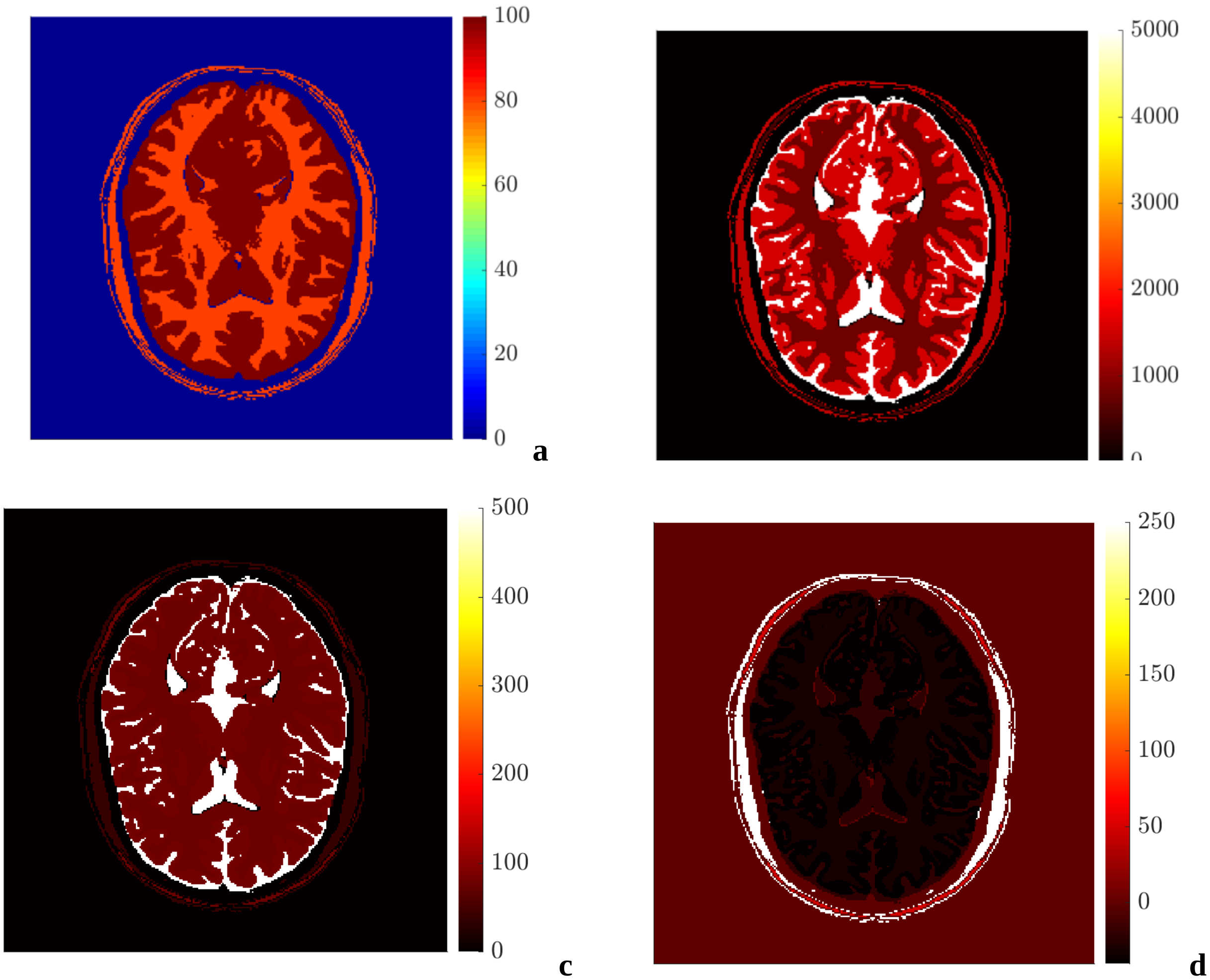

Figure 5. 3: Ground truth brain phantoms:(a) proton density, (b) T1 phantom(ms), (c) T2 phantom(ms), (d) off-resonance (Hz)

5.3 Undersampled Time Series Image Acquisition

The data acquisition step took 16 hours for the EPI acquisition and 14 hours for single interleave spiral acquisition of time series images.

5.3.1 Acquired data for cylindrical phantoms

The first four highly undersampled images from the series of 1000 images acquired using a single interleave spiral trajectory and sixteen-shot EPI are shown in Fig. 5.4. The data is acquired using the simulator and pulse sequence described in Chapter 4. One typical voxel's temporal signal evolution curve for the whole time series of 1000 repetition is shown in Fig. 5.6. Despite the fact that subsampling artifacts dominate both the cylindrical and brain phantom images, the matching algorithm is able to find the corresponding dictionary entry that has the greatest correlation with the acquired data. This demonstrates the algorithm's robustness to undersampling artifacts.

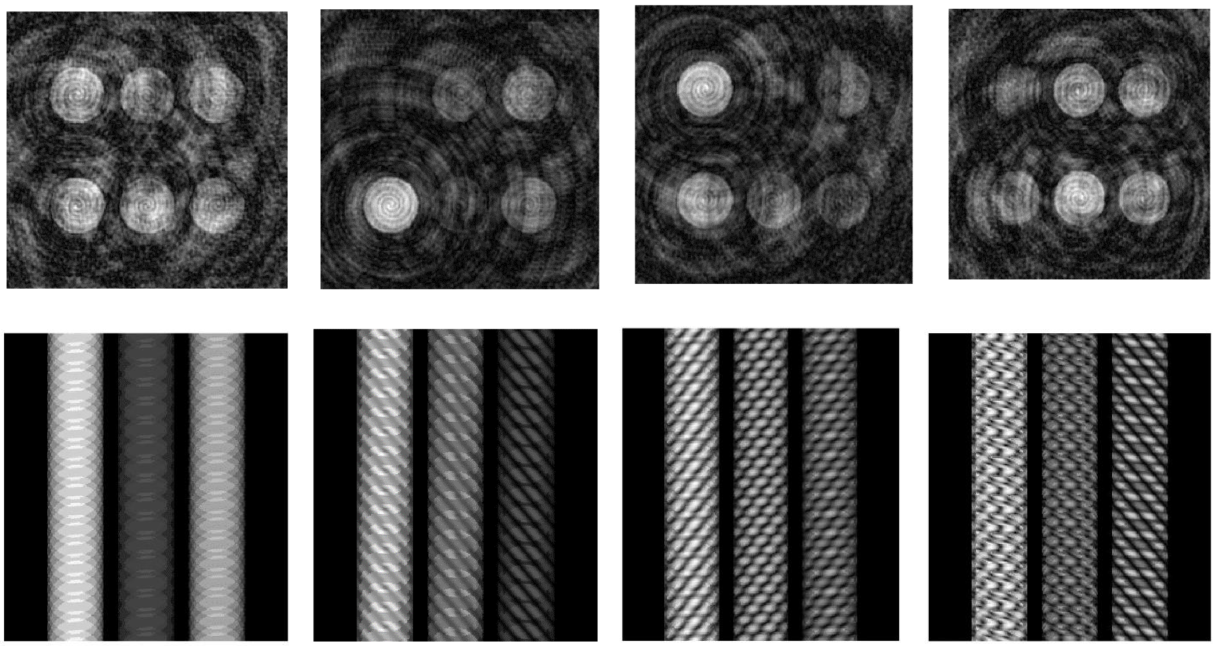

Figure 5. 4*: The first 4 highly aliased time series images acquired using spiral trajectory (top row) and EPI (bottom row)*

5.3.2 Acquired data for brain phantoms

The first four highly undersampled brain images from the series of 1000 images acquired using a single interleave spiral trajectory and sixteen-shot EPI are shown in Fig. 5.5..

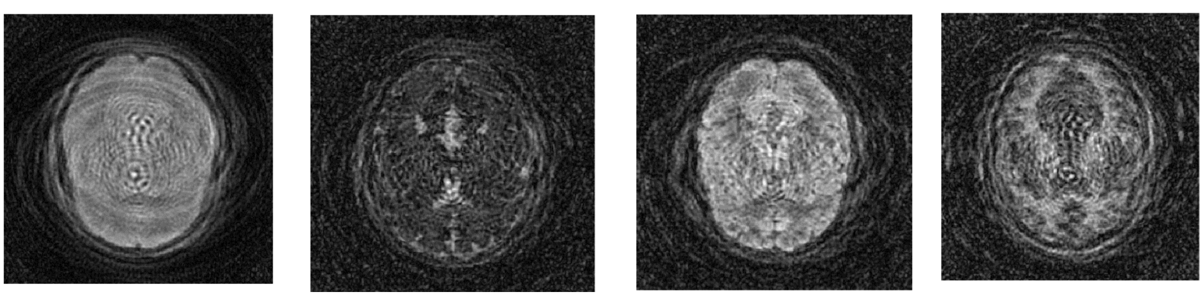

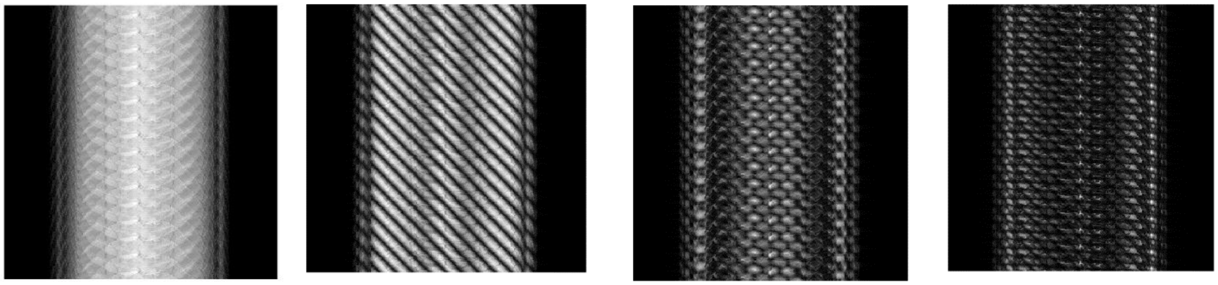

Figure 5. 5: *The first 4 highly aliased time series images acquired using spiral trajectory (top row) and EPI (bottom row)*

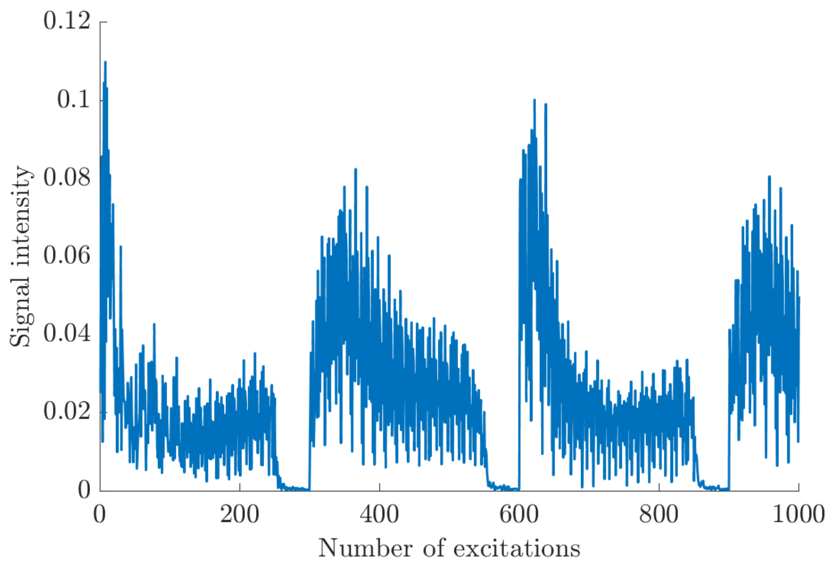

Figure 5. 6: *Signal evolution curve for a typica single voxel*

5.4 Pattern Recognition and Visualization

The pattern recognition step in both experiments took 7 minutes. The parametric maps for the spiral MRF are visually similar to the ground truth maps. While for EPI-MRF, the results are not visually similar with the ground truth maps. The mean T1, T2 and off-resonance values for spiral-MRF are in good agreement with the ground truth with percentage errors of 2.6%, 2.3% and 14% respectively. The mean T1, T2 and off-resonance values for the EPI-MRF are not in agreement with the ground truth with percentage error of 39%, 43%, 124% respectively.

5.4.1 Results for cylindrical phantoms

Figure 5.7 shows comparison of the T1, T2 and off-resonance maps for spiral MRF and EPI-MRF along with the ground truth values for the cylindrical phantom experiment. Tables 5.1, 5.2, and 5.3

show the mean T1, T2 and off-response frequencies for the six cylindrical regions of interest, respectively. The corresponding bar graphs can be seen in Figures 5.8, 5.9 and 5.10.

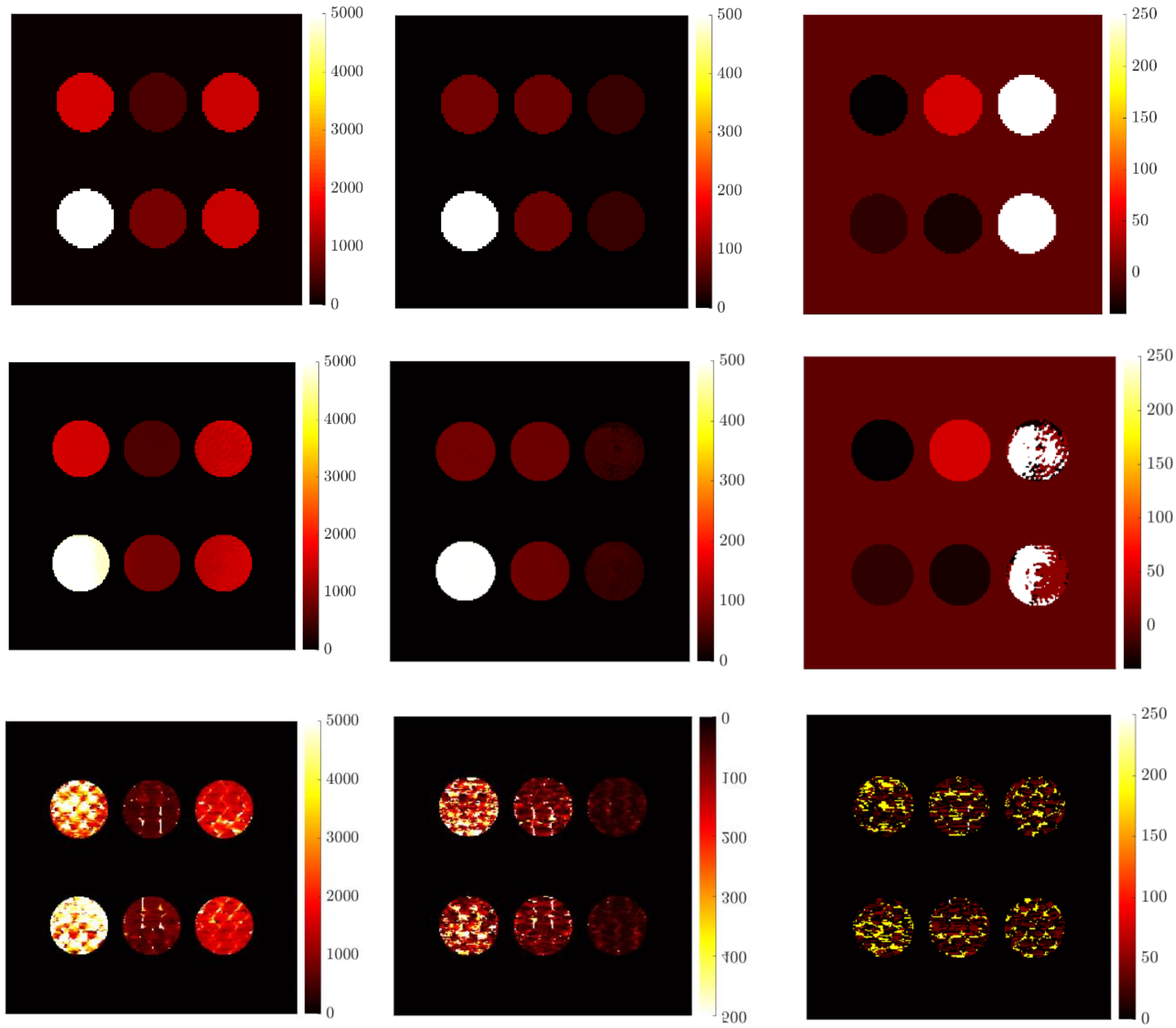

T1 map **T2 map** **df map**

Figure 5. 7: *T1, T2 and off-resonance(df) maps using cylindrical phantoms: ground truth (top row), generated using spiral-MRF (middle row) and EPI-MRF (bottom row)*

	C1	**C2**	**C3**	**C4**	**C5**	**C6**
GT	5.012	1.545	0.811	0.530	1.425	1.425
Spiral-MRF	4.9467	1.5312	0.8543	0.5588	1.4412	1.4491
EPI-MRF	4.4485	3.5105	0.9069	0.6887	1.7783	1.8659

Table 5. 1: *The mean T1 values of the six cylinders in seconds (C1, C2, C3, C4, C5, C6) in the cylindrical phantom experiment, comparing i) Ground Truth (GT), ii) spiral-MRF and iii) EPI-MRF*

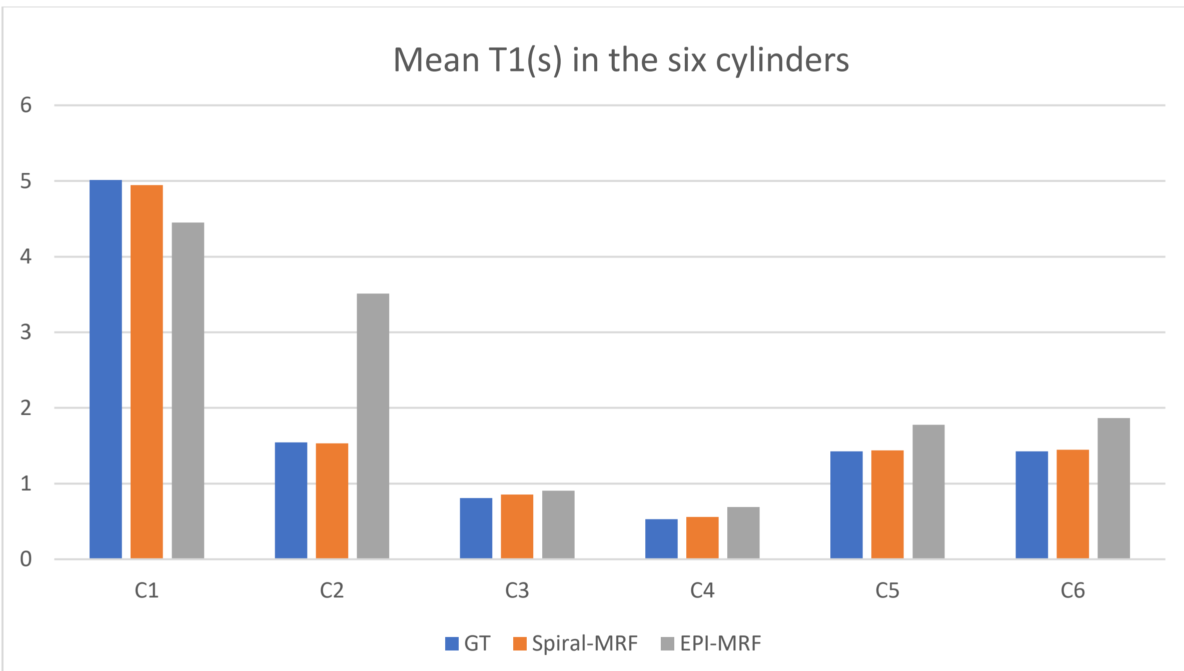

Figure 5. 8: *Bar chart of the mean T1 values in seconds of the six cylindrical regions of the ground truth, spiral-MRF and EPI-MRF maps.*

	C1	**C2**	**C3**	**C4**	**C5**	**C6**
GT	0.512	0.083	0.077	0.077	0.041	0.041
Spiral-MRF	0.5034	0.0829	0.0778	0.0795	0.0395	0.0392
EPI-MRF	0.2566	0.1943	0.1048	0.0936	0.0362	0.0368

Table 5. 2: *The mean T2 values of the six cylinders (C1, C2, C3, C4, C5, C6) in the cylindrical phantom experiment, comparing i) Ground Truth (GT), ii) spiral-MRF and iii) EPI-MRF*

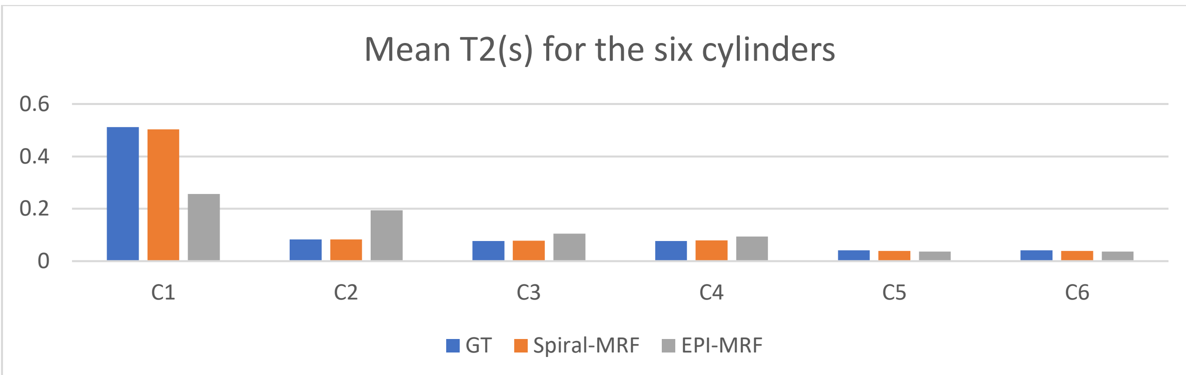

Figure 5. 9: *Bar chart of the mean T2 values in seconds of the six cylindrical regions of the ground truth, spiral-MRF and EPI-MRF maps.*

	C1	C2	C3	C4	C5	C6
GT	-20	-40	-30	50	250	250
Spiral-MRF	-20	-40	-30	50	134.28	146.48
EPI-MRF	22.0879	18.4741	13.8100	15.6317	26.7218	27.9680

Table 5. 3: *The mean off-resonance values of the six cylinders (C1, C2, C3, C4, C5, C6) for the cylindrical phantom experiment, comparing i) Ground Truth (GT), ii) spiral-MRF and iii) EPI-MRF*

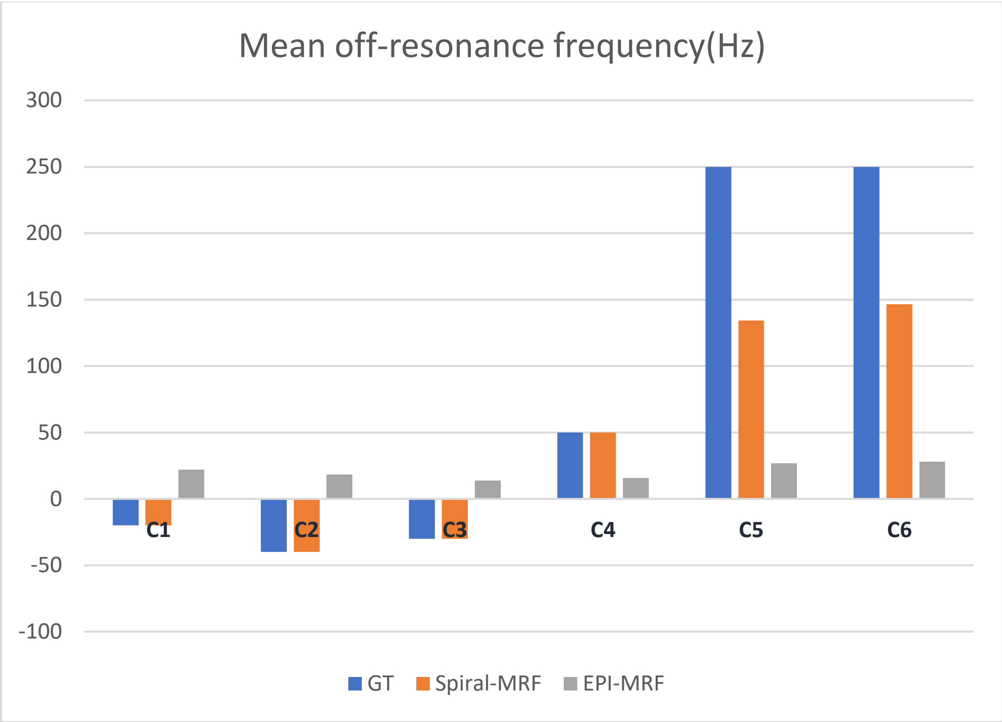

Figure 5. 10: *Bar chart of the mean off-resonance frequencies in Hz of the six cylindrical regions of the ground truth, spiral-MRF and EPI-MRF maps.*

5.4.22 Results for brain phantoms.

Figure 5.11 shows comparison of the T1, T2 and off-resonance maps for spiral MRF and EPI-MRF along with the ground truth values respectively for the brain phantom experiment. In this experiment the parameter maps of grey matter and white matter are compared. The mean T1, T2 and off-resonance frequencies can be seen on Tables 5.4, 5.5, and 5.6 respectively with corresponding bar graphs in Figures 5.12, 5.13, 5.14**.**

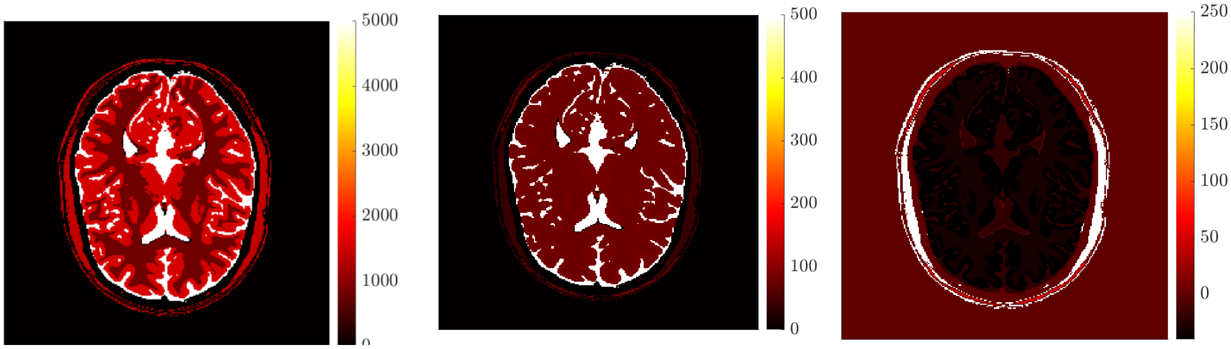

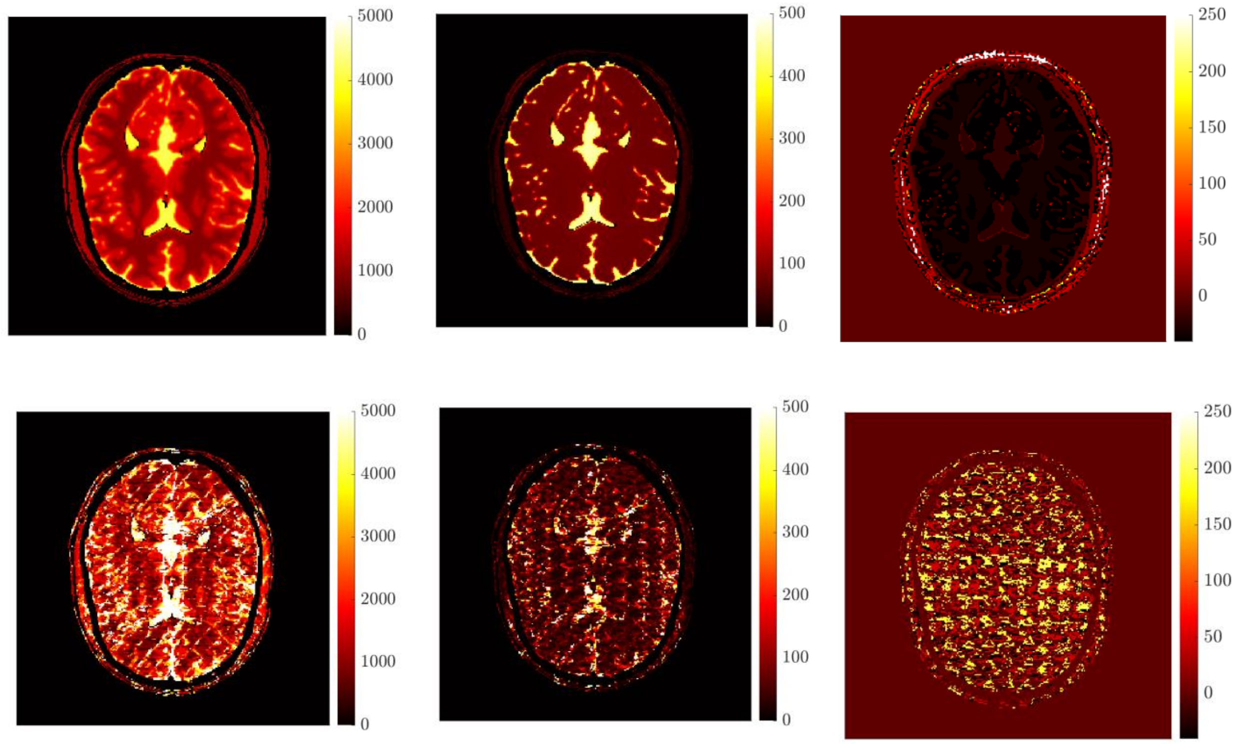

T1 map **T2 map** **df map**

Figure 5. 11*: T1, T2 and off-resonance maps using brain: ground truth (top row), generated using spiral-MRF (middle row) and EPI-MRF (bottom row).*

	Grey Matter (GM)	**White Matter (WM)**
GT	1.545	0.811
Spiral-MRF	1.5771	1.0558
EPI-MRF	2.2969	1.5370

Table 5. 4: *The mean T1 values of Grey Matter (GM) and White Matter (WM) for the brain phantom experiment, comparing i) Ground Truth (GT), ii) spiral-MRF and iii) EPI-MRF*

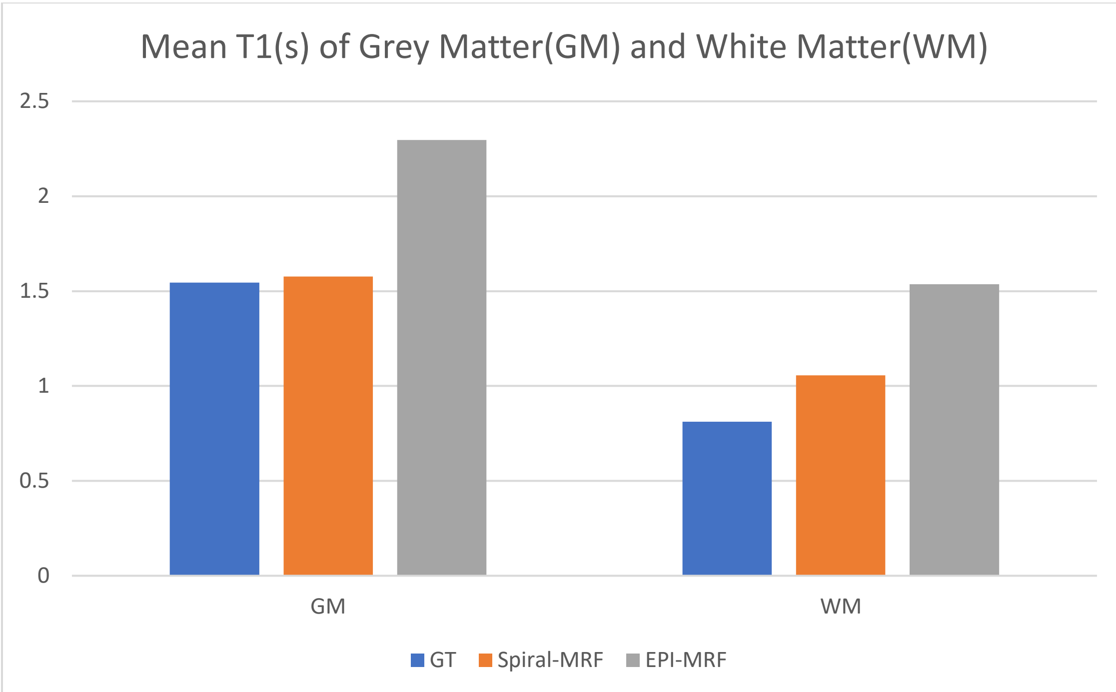

Figure 5. 12: *Bar chart of the mean T1 values(seconds) of grey matter and white matter of the ground truth, spiral-MRF and EPI-MRF maps.*

	Grey Matter (GM)	**White Matter (WM)**
GT	0.083	0.077
Spiral-MRF	0.0918	0.0821
EPI-MRF	0.0850	0.0634

Table 5. 5: *The mean T2 values of Grey Matter (GM) and White Matter (WM) for the brain phantom experiment, comparing i) Ground Truth (GT), ii) spiral-MRF and iii) EPI-MRF*

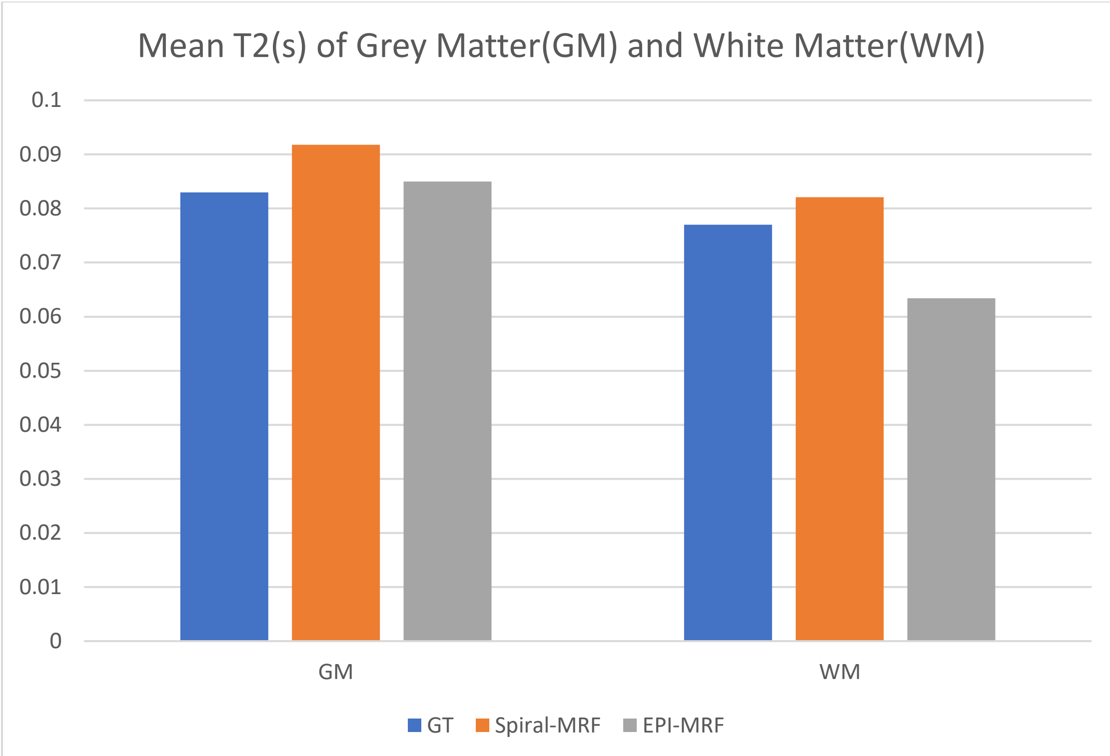

Figure 5. 13: *Bar chart of the mean T2 values(seconds) of grey matter and white matter of the ground truth, spiral-MRF and EPI-MRF maps.*

	Grey Matter (GM)	**White Matter (WM)**
GT	-40	-30
Spiral-MRF	-38.0856	-30.0490
EPI-MRF	22.0523	22.7934

Table 5. 6: *The mean off-resonance values of Grey Matter (GM) and White Matter (WM) for the brain phantom experiment, comparing i) Ground Truth (GT) ii) spiral-MRF iii) EPI-MRF.*

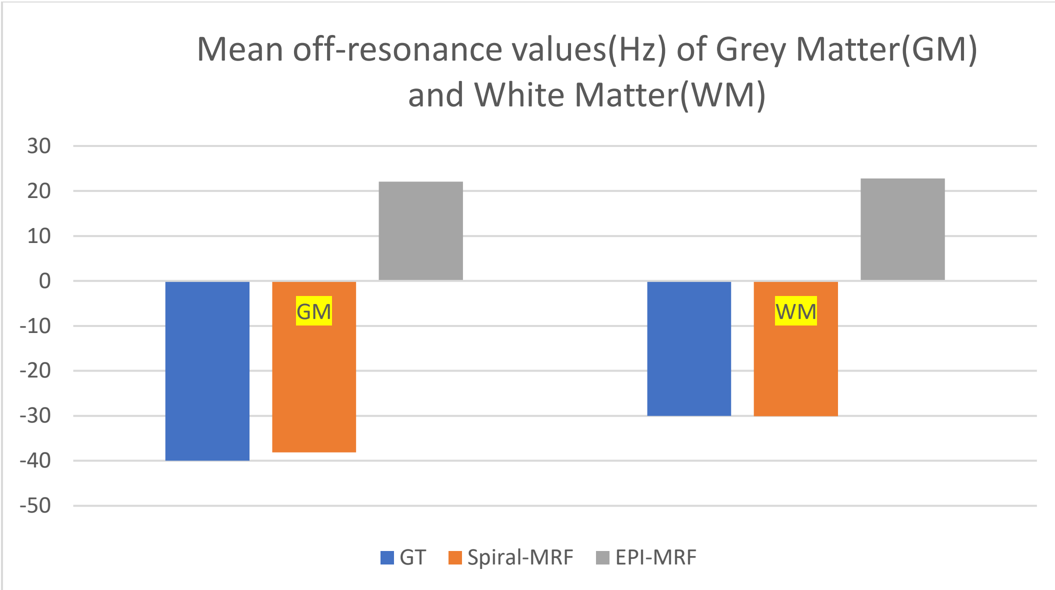

Figure 5. 14: *Bar chart of the mean off-resonance frequencies (Hz) of grey matter and white matter of the ground truth, spiral-MRF and EPI-MRF maps.*

5.4 Discussion

In this thesis, the MRF method has been studied using undersampled data acquisition with spiral and EPI trajectories; an accurate MRF simulator has been built that includes the effect of magnetic fields on the acquired signal; generated a dictionary accurately simulating signal evolution for bSSFP sequence; compared the undersampling capabilities of EPI and spiral sampling. Despite significant undersampling artifacts present in the acquired time series images, the pattern-matching algorithm was able to identify the dictionary entry with the highest correlation to the acquired data. This shows the algorithm's ability to withstand the effects of undersampling artifacts. Although the undersampling artifact in EPI are regular because of the uniform undersampling, the temporal signal evolution is random like the spiral sampling case which can be identified by the pattern-matching algorithm. The randomness of the signal in the temporal domain facilitates effective discrimination between dictionary elements resulting in an accurate dictionary matching.

In both cylindrical and brain phantom experiments, good quantification of T1, T2 and off-resonance maps has been accomplished for the spiral trajectory in k-space. While in the case of EPI trajectory, the results were not accurate. The generated maps are also in good agreement with the ground truth phantom maps for spiral trajectory. The reason for good performance of spiral trajectory is due to dense sampling around the k-space origin. Spiral trajectory has great potential to be used as an effective tool in MRF. On comparison of the maps, as shown in Fig. 5.7 and 5.11, T1 maps showed best accuracy while df maps are poorly quantified in both methods. This is because of the high T1 sensitivity of the encoding strategy. More discrepancy in the off-resonance map is particularly witnessed at higher frequencies. Since the full k-space (including high frequency data from the k-space corners) is sampled in EPI, using iterative reconstruction could result in better performance. It is generally difficult to do pattern recognition based on dot products when we have the digital phantom data containing only single coil data. This is true when using any sampling method including the spiral as well as the EPI approaches used in the current study. Using multi-coil data can produce better results.

In terms of efficiency during reconstruction of the series images, spirally sampled images took more time due to the computationally more expensive NUFFT algorithm than EPI's FFT. However, the overall efficiency of the spiral approach was considerably better than the EPI (14 hours vs 16 hours in our case).

Current MRF simulators, such as [46], do not simulate the effect of magnetic fields, including gradients, Bo, and B1 in the acquisition of the undersampled series images. These simulators simply use the Fourier transform (FFT) to transform phantoms into the frequency domain without actually simulating the sampling of the signal while applying the gradients as the signal evolves. They also do not simulate the application of Bo and B1, instead use the analytical Bloch equation to compute the effect of application of these fields. To undersample the data, these simulators zero-fill the lines of k-space that are not supposed to be sampled. However, this kind of simulation is not an accurate representation of the real process in MR image acquisition. The simulator proposed in the current thesis work accurately simulates the effect of magnetic fields on spins and on the sampled signal. It can accurately simulate the acquisition of images on a real MRI scanner. The resulting quantitative maps obtained in this simulator are also similar to results obtained from real MRI machines, as reported in [46, 19]. Although the simulator developed in this study achieved better accuracy than previous simulators, it is based on the single isochromatic method, which assumes that the flip angle and off-resonance frequencies are homogeneous within a voxel. This can be considered as one limitation of the simulator.

Although MRF has a lot of potentials and benefits, there are still important underlying disadvantages to T1 and T2 quantification through the MRF framework. When T1 and T2 values are very high (T1 > 2500ms and T2 > 400ms), the quantification is inaccurate in MRF because it is impossible to distinguish between dictionary entries at these values due to the resolution taken at these high values. However, generating a high-resolution dictionary, which is required for accurate quantification, can result in high computational costs. At the same time, the accuracy of parameter estimation depends directly on the resolution of the simulated dictionary used to perform the matching procedure. As a result, the inaccuracies in parameter mapping can be attributed to the low resolutions of the parameters. The current work was meant only to compare the performance of the two undersampling methods and the issue with the reconstruction accuracy was beyond its scope. The current work also does not fully take into consideration the numerous correction factors used to increase the quantitative accuracy in typical MRF models.

Chapter 6: Conclusion and Recommendation

6.1 Conclusion

In this thesis, an investigation was conducted to compare the performance of the two most common trajectories in k-space during the data acquisition step of magnetic resonance fingerprinting utilizing the dot product-based pattern recognition technique. The results of this study demonstrated that while both trajectories exhibited a notable reduction in data acquisition time, the spiral trajectory outperformed the EPI trajectory in terms of generating more accurate results. Specifically, it was observed that the EPI trajectory failed to produce quantitative maps with the desired level of accuracy. In contrast, the spiral trajectory yielded improved outcomes, which can be attributed to its ability to acquire a higher number of samples from the central region of the k-space, known as the dc value. This strategic sampling approach allows for capturing more information from the critical components of the signal and enhances the fidelity of the resulting quantitative maps. However, despite the enhanced performance of the spiral sampling technique, there is still room for further refinement and improvement in achieving a closer agreement with the ground truth. This indicated that additional research and development efforts are necessary to optimize the parameters and techniques associated with spiral sampling, with the ultimate goal of enhancing its accuracy and reliability.

Additionally, an integral contribution of this thesis is the development of a simulator that accurately replicates the real MR data acquisition process, taking into account the effects of gradient fields on spins. The simulator demonstrated high accuracy and fidelity in simulating MR data acquisition, providing a valuable tool for future MRF studies. This simulator serves as a critical stepping stone for advancing MRF research, enabling researchers to assess and refine various acquisition strategies, optimize parameters, and explore new avenues for improving the overall performance and reliability of MRF techniques.

Overall, this thesis sheds light on the comparative performance of different trajectories in MR fingerprinting and underscores the significance of strategic sampling. It also lays the foundation for future studies to further enhance the accuracy of spiral sampling and highlights the importance of the developed simulator as a valuable resource in advancing MRF research

6.2 Future Work

This thesis has brought to light a variety of subjects that would benefit from more study. Before the MRF framework can be widely accepted in a clinical setting, several key challenges must be addressed. These challenges encompass a large dictionary size, accurate parameter evaluation, and resilience to noise. In MRI, confounding factors like B0 and B+ field inhomogeneities are recognized sources of artifacts. Consequently, future work should account for these factors within the simulator to enhance parameter estimation. One of the challenges in MRF is dealing with the large size of this dictionary during multi-parametric mapping with high-resolution parameters, which can be computationally demanding. More study into efficient ways to handle and optimize the dictionary size is crucial for practical implementation. Furthermore, to overcome the limitations of dictionary-based template matching, it is imperative to delve into the realm of Machine Learning. By exploring algorithms based on supervised learning, a robust approach can be developed. One viable method involves utilizing a pre-trained model that can predict MR parameters when provided with an experimental fingerprint as input. Among the wide range of machine learning algorithms, Neural Networks stand out as an ideal choice for this task. Their universal function approximation capability, combined with the ability to handle large amounts of training data and intricate model complexities, make Neural Networks particularly well-suited for this purpose.

Accurately estimating parameters from MRF data is another challenge. The MRF framework requires robust algorithms to extract the desired parameters from the acquired signals. In this regard, iterative reconstruction methods need to be further studied. The noise from MR scanners also affects the accuracy of parameter estimation in MRF. Developing noise-robust techniques and algorithms that can handle and mitigate the impact of noise on parameter estimation should also be considered. Further study into the simulator from this study should take into account various noise sources for better accuracy.

The simulator developed in the current study has inherent numerical errors associated with the iterative application of the gradients and other magnetic fields. Future work should focus on refining the simulator to minimize these errors, which could lead to more accurate and reliable results. Moreover, the simulator only simulates 2D scans. To make it more comprehensive and representative of real scenarios, more work is required to incorporate 3D data acquisition. This enhancement would enable the simulation to capture volumetric information and provide a more complete representation of the scanning process. Since the MR image acquisition process is a repetitive process, one additional area that needs improvement is the reduction of data acquisition time. This can be achieved by implementing parallel processing techniques and utilizing Graphical Processing Units (GPUs). These technologies can significantly speed up the computation process, allowing for faster data acquisition and reconstruction. These and similar other issues with the current study require further investigations

References

[1] V. Gulani and N. Seiberlich, "Quantitative MRI: Rationale and Challenges," *Advances in Magnetic Resonance Technology and Applications*, vol. 1, pp. xxxvii-li, 2020.

[2] C. Pierpaoli, "Quantitative Brain MRI," *Topics in Magnetic Resonance Imaging,* vol. 21, no. 2, p. 63, 2010.

[3] S. Barbosa, L. Blumhardt, N. Roberts, T. Lock and R. Edwards, "Magnetic resonance relaxation time mapping in multiple sclerosis: normal appearing white matter and the “invisible”lesion load.," *Magn. Reson. Imaging,* vol. 12, p. 33–42, 1994.

[4] M. Eis, T. Els and M. HoehnüBerlage, "High resolution quantitative relaxation and diffusion MRI of three different experimental brain tumors in rat.," *Magn. Reson. Med.,* vol. 34, p. 835–844, 1995.

[5] P. Martin, B. Bender and N. Focke, "Post-processing of structural MRI for," *Quant. Imaging Med. Surg.,* vol. 5, p. 188–203, 2015.

[6] S. C. L. Deoni, T. M. Peters and B. K. Rutt, "High-resolution T1 and T2 mapping of the brain in a clinically acceptable time with DESPOT1 and DESPOT2," *Magn. Reson. Med.,* vol. 53, p. 237–241, 2005.

[7] I. Dregely, D. Margolis, K. Sung, Z. Zhou, N. Rangwala, S. Raman and H. Wu, "Rapid quantitative T2 mapping of the prostate using three-dimensional dual echo steady state MRI at 3T," *Magn. Reson. Med.,* vol. 76, p. 1720–1729, 2016.

[8] C. Liao, B. Bilgic, M. Manhard, B. Zhao, X. Cao, J. Zhong, L. Wald and K. Setsompop, "3D MR fingerprinting with accelerated stack-of-spirals and hybrid sliding-window and GRAPPA reconstruction," *NeuroImage,* vol. 30, no. 08, 2017.

[9] S. C. L. Deoni, "Quantitative relaxometry of the brain," *Topics in Magnetic Resonance Imaging* , pp. 233-241, 2016.

[10] D. Ma, V. Gulani, N. Seiberlich, K. Liu, J. Sunshine, J. Duerk and M. Griswold, "Magnetic resonance fingerprinting," *Nature,* vol. 495, p. 187–192, 2013.

[11] F. Bloch, "Nuclear induction," *Phys Rev,* vol. 70, p. 460–474, 1946.

[12] R. Summers, L. Axel and S. Israel, "A computer simulation of nuclear magnetic resonance," *Magn Reson Med*, vol. 3, p. 363–376, 1986.

[13] O. MBE, W. R and P. BRR., "A computer simulation program for mr imaging: application to rf and static magnetic field imperfections," *Magn Reson Med,* vol. 34, p. 612–617, 1995.

[14] "Yoder DA, Zhao Y, Paschal CB, Fitzpatrick JM.," *MRI simulator with object-specific field map calculations,* vol. 22, p. 315–328, 2004.

[15] I. Drobnjak, D. Gavaghan, E. Suli, J. Pitt-Francis and M. Jenkinson, "Development of a functional magnetic resonance imaging simulator for modeling realistic rigid-body," *Magn Reson Med,* vol. 56, p. 364–380, 2006.

[16] T. Stocker, K. Vahedipour, D. Pflugfelder and N. Shah, "High-performance computing MRI simulations," *Magn Reson Med,* vol. 64, p. 186–193, 2010.

[17] F. Liu, J. Velikina, W. Block, R. Kijowski and A. Samsonov., "Fast Realistic MRI Simulations Based on Generalized Multi-Pool Exchange Tissue Model.," *IEEE Transactions on Medical Imaging,* vol. 36, no. 2, pp. 527 - 537, 2016.

[18] N. Dikaios, N. E.Protonotarios, A. S.Fokas and G. A.Kastis, "Quantification of T1, T2 relaxation times from Magnetic Resonance Fingerprinting radially undersampled data using analytical transformations," *Magnetic Resonance Imaging,* vol. 80, pp. 81-89, 2021.

[19] A. J. V. Benjamin, P. A. Gómez, M. Golbabaee, Z. B. Mahbub, T. Sprenger, M. I. Menzel, M. Davies and I. Marshall, "Multi-shot Echo Planar Imaging for accelerated Cartesian MR Fingerprinting: An alternative to conventional spiral MR Fingerprinting," *Magnetic Resonance Imaging,* vol. 61, pp. 20-32, 2019.

[20] Klaus Scheffler, Stefan Lehnhardt, "Principles and applications of balanced SSFP techniques," *Eur Radiol.,* vol. 13, p. pages2409–2418, 2003.

[21] O. Glenn and J. Barkovich, "Magnetic Resonance Imaging of the Fetal Brain and Spine: An Increasingly Important Tool in Prenatal Diagnosis: Part 2," *American Journal of Neuroradiology,* vol. 27, no. 9, pp. 1807-1814, 2006.

[22] W. J. Chung, H. W. Chung, M. J. Shin, S. H. Lee, M. H. Lee, J. S. Lee, M.-J. Kim and W. K. Lee, "MRI to differentiate benign from malignant soft-tissue tumours of the extremities: a simplified systematic imaging approach using depth, size and heterogeneity of signal intensity," *Br J Radiol.,* vol. 85, no. 1018, p. 831–836, 2012.

[23] E. E, O'Connor, L. B. Dixon, T. Peabody and G. S. Stacy, "MRI of Cystic and Soft-Tissue Masses of the Shoulder Joint," *American Journal of Roentgenology,* vol. 183, no. 1, pp. 39-47, 2004.

[24] T. Schenberg, G. Mitchell, D. Taylor and C. Saunders, "MRI screening for breast cancer in women at high risk; is the Australian breast MRI screening access program addressing the needs of women at high risk of breast cancer?," *J Med Radiat Sci,* vol. 62, no. 3, p. 212–225., 2015.

[25] A. G. J. Niu, D. Hayashi, F. W. Roemer, M. Englund, T. Neogi, P. Aliabadi, C. E. McLennan and D. T. Felson, "Prevalence of abnormalities in knees detected by MRI in

adults without knee osteoarthritis: population based observational study (Framingham Osteoarthritis Study)," *BMJ,* vol. 345, p. 5339, 2012.

[26] M. Saeed, T. A. Van, R. Krug, S. W. Hetts and M. W. Wilson, "Cardiac MR imaging: current status and future direction," *Cardiovascular Diagnosis and Therapy (CDT),* vol. 5, no. 4, 2015.

[27] B. Taouli, R. L. Ehman and S. B. Reeder, "Advanced MRI Methods for Assessment of Chronic Liver Disease," *American Journal of Roentgenology,* vol. 193, no. 1, pp. 14-27, 2009.

[28] S. B. Grover, N. Antil, A. Katyan, H. Rajani, H. Grover, P. Mittal and S. Prasad, "Niche role of MRI in the evaluation of female infertility," *Indian Journal of Radiology and Imaging,* vol. 30, no. 1, pp. 32-45, 2020.

[29] A. M. Kennedy, M. R. Gilfeather and P. J. Woodward, "MRI of the female pelvis," *Seminars in Ultrasound, CT and MRI,* vol. 20, no. 4, pp. 214-230, 1999.

[30] V. Pasoglou, N. Michoux, A. Larbi, S. V. Nieuwenhove and F. Lecouvet, "Whole Body MRI and oncology: recent major advances," *The British Journal of Radiology,* vol. 91, no. 1090, 2018.

[31] Nishimura and D. G, Principles of Magnetic Resonance Imaging, Stanford, CA 94305, USA: Stanford Univ, 2010.

[32] H. EM, B. RW, T. MR and V. R, Magnetic resonance imaging: physical principles and sequence design, John Wiley & Sons, 1999.

[33] D. C. Look and D. R. Locker, "Time Saving in Measurement of NMR and EPR Relaxation Times," *Review of Scientific Instruments,* vol. 41, no. 2, p. 250, 1970.

[34] A. D. Elster, "Myocardio T1 mapping,," Elster LLC, [Online]. Available: https://mriquestions.com/t1-mapping.html. [Accessed 2023].

[35] W. Li, M. A. Griswold and X. Yu, "Rapid T1 mapping of mouse myocardium with," *Magnetic Resonance in Medicine,* vol. 64, pp. 1296-1303, 2010.

[36] P. Schmitt, M. A. Griswold, P. M. Jakob, M. Kotas, V. Gulani and M. F. a. A., "Inversion recovery TrueFISP: quantification of T1, T2, and spin density," *Magnetic Resonance in Medicine,* vol. 51, pp. 661-667, 2004.

[37] A. Panda, B. B. M. S. C. Y. Jiang, D. M. N. Seiberlich and M. A. G. V. Gulani, "Magnetic Resonance Fingerprinting-An Overview," *Curr Opin Biomed Eng,* vol. 3, pp. 56-66, 2017.

[38] S. Buonincontri and G. Sawiak, "MR fingerprinting with simultaneous B1 estimation," *Magn Reson Med,* vol. 76, p. 1127–1135, 2016.

[39] M. M. Cloos, F. Knoll, T. Zhao, K. B. Block, G. Wiggins and S. DK, "Multiparametric imaging with heterogeneous radiofrequency fields," *Nat Commun,* 2016.

[40] B. Rieger, F. Zimmer, J. Zapp, S. Weingärtner and L. Schad, "Magnetic resonance fingerprinting using echo-planar imaging: joint quantification of T1 and T2* relaxation times," *Magn Reson Med,* vol. 78, p. 1724–1733, 2016.

[41] P. Su, D. Mao, P. Liu, Y. Li, M. Pinho, B. Welch and H. Lu, "Multiparametric estimation of brain hemodynamics with MR fingerprinting ASL," *Magn Reson Med,* vol. 2017, p. 1812–1823, 2017.

[42] D. Wang, J. Ostenson and D. S.Smith, "snapMRF: GPU-accelerated magnetic resonance fingerprinting dictionary generation and matching using extended phase graphs," *Magnetic Resonance Imaging,* vol. 66, pp. 248-256, 2020.

[43] A. J. V. Benjamin, P. A. Gómez, M. Golbabaee, Z. B. Mahbub, T. Sprenger, M. I. Menzel, M. Davies and I. Marshall, "Multi-shot Echo Planar Imaging for accelerated Cartesian MR," *Magnetic Resonance Imaging,* vol. 61, pp. 20 - 32, 2019.

[44] D. F. McGivney, E. Pierre, D. Ma, Y. Jiang, H. Saybasili, V. Gulani and M. A. Griswold, "SVD Compression for Magnetic Resonance Fingerprinting in the Time Domain," *IEEE TRANSACTIONS ON MEDICAL IMAGING,* vol. 33, 2014.

[45] D. M., P. G., V. P. and W. a. Y., "A compressed sensing framework for magnetic resonance fingerprinting," *SIAM Journal on Imaging Sciences,* vol. 7, 2014.

[46] M. Golbabaeey, Z. Chen, Y. Wiau and M. Davies, "CoverBLIP accelerated and scalable iterative matched-filtering for Magnetic Resonance Fingerprint," *Inverse Problems,* vol. 36, 2019.

[47] P. Virtue, S. Yu and M. Lustig, "Better than real: complex-valued neural nets for MRI fingerprinting," in *IEEE International Conference on Image Processing,* 2017.

[48] C. O, Z. B and R. MS, "MR fingerprinting Deep RecOnstruction NEtwork (DRONE)," *Magn Reson Med,* vol. 80, pp. 885-894, 2018.

[49] Y. Chen, Z. Fang, S. Hung, W. Chang, D. Shen and W. Lin, "Highresolution 3D MR fingerprinting using parallel imaging and deep learning," *Neuroimage,* vol. 206, 2020.

[50] Z. Fang, Y. Chen, S. Hung, X. Zhang, W. Lin and D. Shen, "Submillimeter MR fingerprinting using deep learning-based tissue quantification," *Magn Reson Med,* vol. 848, pp. 579-591, 2020.

[51] Y. Jiang, D. Ma, N. Seiberlich and 1. a. M. A. G. Vikas Gulani, "MR Fingerprinting Using Fast Imaging with Steady State Precession (FISP) with Spiral Readout," *Magn Reson Med,* vol. 74, no. 6, pp. 1621-31, 2014.

[52] D. F. McGivney, Eric Pierre, D. Ma, Y. Jiang, H. Saybasili, V. Gulani and M. A. Griswold, "SVD compression for magnetic resonance fingerprinting in the time domain," *IEEE Trans Med Imaging,* vol. 33, no. 12, pp. 2311-22, 2014.

[53] M. A. Cloos, F. Knoll, T. Zhao, K. T. Block, M. Bruno, G. C. Wiggins and D. K. Sodickson, "Multiparametric imaging with heterogeneous radiofrequency fields," *Nat Commun,* vol. 7, p. 12445, 2016.

[54] J. Assländer, S. J. Glaser and J. Hennig, "Pseudo Steady-State Free Precession for MR-Fingerprinting," *Magn Reson Med,* vol. 77, no. 3, p. 2017, Magn Reson Med.

[55] G. Buonincontri and S. J. Sawiak, "MR fingerprinting with simultaneous B1 estimation," *Magn Reson Med,* vol. 76, no. 4, pp. 1127-35, 2016.

[56] T. Christen, N. A. Pannetier, W. W. Ni, D. Qiu, M. E. Moseley, N. Schuff and G. Zaharchuk, "MR vascular fingerprinting: A new approach to compute cerebral blood volume, mean vessel radius, and oxygenation maps in the human brain," *Neuroimage,* vol. 89, pp. 262-70, 2014.

[57] C. C. Stolk and A. Sbrizzi, "Understanding the Combined Effect of k -Space Undersampling and Transient States Excitation in MR Fingerprinting Reconstructions," *IEEE Trans Med Imaging,* vol. 38, no. 10, pp. 2445-2455, 2019.

[58] C. Badve, A. Yu, M. Rogers, D. Ma, Y. Liu, M. Schluchter and J. Sunshine, "Simultaneous T1 and T2 brain relaxometry in asymptomatic volunteers using magnetic resonance fingerprinting," *Tomogr J Imaging Res,* vol. 1, p. Tomogr J Imaging Res, 2015.

[59] C. Badve, A. Yu, S. Dastmalchian, M. Rogers, D. Ma and J. Y, "MR fingerprinting of Adult brain tumors: initial experience," *AJNR Am J Neuroradiol,* vol. 38, p. Neuroradiol, 2017.

[60] Y. AC, C. Badve, L. Ponsky, S. Pahwa, S. Dastmalchian, A. Yu, C. Badve, L. Ponsky, S. Pahwa and S. Dastmalchian, "Development of a combined MR fingerprinting and diffusion examination for prostate cancer," *Radiology,* vol. 238, p. 729–738, 2017.

[61] J. Hamilton, Y. Jiang, Y. Chen, D. Ma, W.-C. Lo, M. Griswold and N. Seiberlich, "MR fingerprinting for rapid quantification of myocardial T1, T2, and proton spin density," *Magn Reson Med,* vol. 77, p. 1446–1458, 2017.

[62] T. Christen, N. Pannetier, W. Ni, D. Qiu, M. Moseley, N. Schuff and G. Zaharchuk, "MR vascular fingerprinting: a new approach to Compute cerebral blood volume, mean vessel radius, and oxygenation maps in the human brain," *NeuroImage,* vol. 89, p. 262–270, 2014.

[63] E. Muhammed, "TOWARD A SIMULATION FRAMEWORK FOR," Addis Ababa University, Addis Ababa, 2020.

[64] P.Sutton and F. J. A., "Nonuniform fast Fourier transforms using min_max interpolation," *IEEE Transactions on Signal Processing*, vol. 51, pp. 560 - 574, 2003.

[65] V. K. R.-S. K. A. E. C.A. Cocosco, "BrainWeb: Online Interface to a 3D MRI Simulated Brain Database," *NeuroImage*, vol. 5, no. 4, 1997.

[66] B. Rieger, F. Zimmer, J. Zapp, S. Weingärtner and L. R. Schad, "Magnetic resonance fingerprinting using echo-planar imaging: Joint quantification of T1 and T2 relaxation times," *Magn Reson Med*, vol. 78, no. 5, pp. 1724-1733, 2017.

[67] P. Su, D. M. P. Liu, Y. Li, M. C. Pinho, B. G. Welch and H. Lu, "Multiparametric estimation of brain hemodynamics with MR fingerprinting ASL," *Magn Reson Med*, vol. 78, no. 5, pp. 1812-1823, 2017.

Appendix

Appendix A: The Main Matlab Code of the Simulator

```
clc;clear;close all;clear path
addpath(genpath(pwd));
%% Settings
phantomString= 'brain';
%phantomString= 'custom';
globalVars = globalvars(phantomString);
samplingScheme = 'spiral';
%samplingScheme = 'EPI';

%% Generate gradient and rewinder
switch (samplingScheme)
case 'spiral'
    [k_space,g,time] = spiralInterleaved(3,5);
    [kr,gr] = rewinder(kSpace,g,time,time(end)-time(end-1));
    [allGradientValues, allKspaceValues] =
generateAllTrajectories(gr,kr);%rotate the spiral
case 'EPI'
    gradParas =
gradientDesign(globalVars.FOV,globalVars.BANDWIDTH,globalVars.NUM_PIX_X,global
Vars.NUM_PIX_Y,globalVars.nShot);
end
%% generate phantom
switch (phantomString)
case 'brain'
    [ densityPhantom, T1Phantom, T2Phantom, dfPhantom ] = brainPhantoms;
case 'custom'
[ densityPhantom, T1Phantom,T2Phantom, dfPhantom ] = customPhantoms(256);
end

%% Pulse Sequence
numRep = 1000;
RFpulses = generateRF;
TR = generate_TR(numRep);
%% sampling using discrate bloch simulation
switch (samplingScheome)
    case 'spiral'
        kSpaceSamples = blocSampling(
T1Phantom,T2Phantom,densityPhantom,dfPhantom,time,allGradientValues,RFpulses,T
R,numRep);
    case 'EPI'
        kSpaceSamples = blocSampling(simPara,globalVars,phantoms);
end
 %% Series images reconstruction
 reconImage = zeros(globalVars.NUM_PIX_X,globalVars.NUM_PIX_X,numRep);
 switch (samplingScheme)
    case 'spiral'
        reconImage = reconImages(allKspaceValues,kSpaceSamples);
```

```
    case 'EPI'
        for i = 1:numRep
           reconImage(:,:,i) =
i*ones(10,10);%fftshift(ifft2(fftshift(kSpaceSamples(:,:,i))));
        end
 end
 %% Generate dictionary
 [dictionary,LUT,dictNorm]=generateDict(TR,RFpulses); %build the MRF
dictionary and its matching look up table
 dictionary = single(dictionary);
 %% Pattern matching using inner product
[match,indx,T1Map,T2Map,dfMap]=PatternMatching(dictionary,reconImage,LUT,T1_ph
antom,T2_phantom,density,df_phantom,dictNorm);
```

Appendix B: Matlab Code for Generating Brain Phantoms

```
function [ density, T1_phantom, T2_phantom, df_phantom ] = brainPhantoms()

% load in MNI segmented brain phantom
% MNI segmented brain phantom is segmented into:
%(0=Background, 1=CSF, 2=Grey Matter, 3=White Matter, 4=Fat, 5=Muscle/Skin,
%6=Skin, 7=Skull, 8=Glial Matter, 9=Connective)

 [imaVol,scaninfo] = loadminc('phantom_1.0mm_normal_crisp.mnc'); % volume is
%217   181   181
 Slice = zeros(256,256);
 Slice(21:237,37:217) = imaVol(:,:,90);
 Slice = Slice.*(Slice<6);  % remove skull Glial matter and connective

% Tissue table chosen to match chemicals from Basics of MRI webbook:
 T1 = [0,5012,1545,811,530,1425,1425];
 T2 = [0, 512,83,77,77,41,41];
 pd = [0, 100,100,80,80,80,80];
 df = [0, -20, -40, -30, 50, 250, 250];

 density = zeros(256,256);
 T1_phantom = zeros(256,256);
 T2_phantom = zeros(256,256);
 df_phantom = zeros(256,256);
 for i = 0:6
   i
     density = density+(Slice==i).*pd(i+1);
     T1_phantom = T1_phantom+(Slice==i).*T1(i+1);
     T2_phantom = T2_phantom+(Slice==i).*T2(i+1);
     df_phantom = df_phantom+(Slice==i).*df(i+1);
 end
end
```

Appendix C: Matlab Code for Generating Cylindrical Phantoms

```
function [ density,T1_phantom,T2_phantom, df_phantom ] = customPhantoms()

N = 256; % Matrix size
E = zeros(6,6); %input to matlab funtion phantom :generates a user-defined
%phantom

A = [1 2 3 4 5 6 ]; %the additive intensity value of the ellipse
E(:,1) = A;

a = [.2, .2, .2, .2, .2, .2]; %the length of the horizontal semi-axis of the
%ellipse
E(:,2) = a;

b = [.2,.2,.2,.2,.2,.2]; %the length of the vertical semi-axis of the ellipse
E(:,3) = b;

X0 = [-.5, -.5, .0, .0, .5, .5]; %the x-coordinate of the center of the
%ellipse
E(:,4) = X0;

Y0 = [-.4, .4, -.4, .4, -.4, .4]; % the y-coordinate of the center of the
%ellipse
E(:,5) = Y0;
phi = [0 0 0 0 0 0];
% phi = [pi./2 ,pi./2,pi./2,pi./2,pi./2,pi./2]; %the angle (in degrees)
%between the horizontal semi-axis of the ellipse and the x-axis of the image
E(:,6) = phi;

P = phantom(E,N); % generate segments of circular shape

%% Generate the MRF phantoms based on the segments in P

 T1 = [0,2000,1545,811,530,1425,1425]; % T1 values of the seven regions
 T2 = [0, 512,83,77,77,41,41]; % T2 values of the seven regions
 pd = [0, 100,100,80,80,80,80]; % T3 values of the seven regions
 df = [0, -20, -40, -30, 50, 250, 250]; % T4 values of the seven regions


 density = zeros(N); %
 T1_phantom = zeros(N);
 T2_phantom = zeros(N);
 df_phantom = zeros(N);

 for i = 0:6

     density = density+(P==i).*pd(i+1);
     T1_phantom = T1_phantom+(P==i).*T1(i+1);
     T2_phantom = T2_phantom+(P==i).*T2(i+1);
     df_phantom = df_phantom+(P==i).*df(i+1);
 end
end
```

Appendix D: Matlab Code for Bloch Simulation

```
function [all_samples ] = blocSampling(
T1_phantom,T2_phantom,density,df_phantom,time,g,RFpulses,TR,L)

rf=abs(RFpulses);
rph=angle(RFpulses);

dt= time(end)-time(end-1);
s = numel(g(1,:));
%s = numel(all_gradient_values(1,:));
all_samples = zeros(s,L);
N_pixel = length(density);
M = zeros(N_pixel,N_pixel,3);
M(:,:,3) =  -density;
M = (reshape(M,N_pixel*N_pixel,3)).';
% beta = zeros(256,256);

tic
for i=1:L
 i

    [M , all_samples(:,i)]=
Bloc_Main(M,g(i,:),rf(i),rph(i),dt,T1_phantom,T2_phantom,density,df_phantom);

    rem_time = TR(i)- dt*s;

    beta = df_phantom.* rem_time*2*pi;
    M = rotate(M,beta);

    M = relax(M,rem_time,T1_phantom,T2_phantom,density); %

end
end
```

Appendix E: Matlab Code for Generating Dictionary of Estimated Signal Evolutions

```
function [dict, dict_norm, lut] = generateDict(TR, RFpulses)
% (c) Mohammad Golbabaee, 2017
L = size(RFpulses,1);

T2=[20:3:100,110:4:200,400:2:600]/1000;
T1=[100:23:2000,2300:301:6000]/1000;
off = [-40:10:50,190:10:250];

counter = 1;
for i = T1
    for j = T2
         if i < j
            continue
         end
        T1_set(counter) = i;
        T2_set(counter) = j;
        counter = counter + 1;
    end
end
d=length(T2_set)*length(off);
T2_set=T2_set.';
T1_set=T1_set.';
% Build lookup table
lookup_table = cell(d, 1);
counter = 1;
for k = off
    for i = T1
        for j = T2
        if i < j
            continue
        end
             lookup_table{counter} = [k i j];
            counter = counter + 1;
        end
    end
end
dict = zeros(d, L);
Dprime=length(T1_set);
for k = 1:numel(off)
    dict((k-1)*Dprime+1:k*Dprime, :) = ...
        fastMRFdictionary_Grisword(RFpulses, TR, T1_set, T2_set, off(k));
end
dict = single(dict);
dict = transpose(dict);
dict_norm =  (sqrt(sum(abs(dict).^2, 1)));
lut=zeros(size(lookup_table,1),3);
for i = 1:size(lookup_table,1)
    lut(i,3) = lookup_table{i}(1);
    lut(i,1) = lookup_table{i}(2);
    lut(i,2) = lookup_table{i}(3);
end
end
```

Appendix F: Matlab Code of the Pattern Matching Algorithm

```
function [match,indx,image,T1_map11,T2_map11,PD_map11,df] =
PatternMatching(D,X,LUT,T1_phantom,T2_phantom,density,df_phantom,dict_norm)
[M,N,~]=size(reconImage);
% dict_norm = sqrt(sum(abs(D).^2,1));
D1 = D./(ones(size(D,1),1)*dict_norm);
X = transpose(reshape(reconImage,N*M,[]));
 x_norm = sqrt(sum(abs(X).^2,1));
 X1 = X./( ones(size(X,1),1)*x_norm );

match = zeros(1, N*M);
indx = match;
tic
for I = 1:N
    I
    [match(1+(I-1)*M:I*M), indx(1+(I-1)*M:I*M)] = max(abs(ctranspose(D1) *
X(:,1+(I-1)*M:I*M)), [], 1);

end

toc
match = max(0, match);
image = D(:,indx(:));
image = image.*repmat(match,[size(image,1),1]);% scale up image
image = reshape(transpose(image), N, M, []);
ind = reshape(indx, N, M);
pd = reshape(match, N, M)./(dict_norm(ind));

T1 = LUT(ind(:),1); T1= reshape(T1, N, M);
T2 = LUT(ind(:),2); T2= reshape(T2, N, M);
if (size(LUT,2)==3)
 df = LUT(indx(:),3); df= reshape(df, N,M);
end
T1_map11 = T1.*(T1_phantom~=0);
T2_map11 = T2.*(T2_phantom~=0);
PD_map11 = pd.*(density~=0);
if (size(LUT,2)==3)
 df_map11 = df.*(df_phantom~=0);%
end


end
% compress sensing site https://web.stanford.edu/class/ee369c/Homework.html
```